The Astrophysical Journal, 894:132 (22pp), 2020 May 10 https://doi.org/10.3847/1538-4357/ab8935

Radiolysis of Ices by Cosmic-Rays: CH_4 and H_2O Ices Mixtures Irradiated by 40 MeV $^{58}Ni^{11+}$ Ions

C. Mejía[1], A. L. F. de Barros[2], H. Rothard[3], P. Boduch[3], and E. F. da Silveira[4]
[1] Facultad de Ciencias Químicas, Universidad de Cuenca, Av. 12 de Abril y Loja, 010202, Cuenca, Ecuador
[2] Departamento de Física, Centro Federal de Educação Tecnológica Celso Suckow da Fonseca, Av. Maracanã 229, 20271-110 Rio de Janeiro, RJ, Brazil
[3] Centre de Recherche sur les Ions, les Matériaux et la Photonique, Normandie Université, ENSICAEN, UNICAEN, CEA, CNRS, CIMAP, F-14000 Caen, France
[4] Departamento de Física, Pontifícia Universidade Católica do Rio de Janeiro, Rua Marquês de São Vicente 225, 22451-900, Rio de Janeiro, RJ, Brazil
Received 2019 February 26; revised 2020 March 28; accepted 2020 April 5; published 2020 May 15

Abstract

Physico-chemical modifications induced by swift heavy ions on methane-water (CH_4:H_2O) ices at 15 K are analyzed. Ice films, at concentrations of (1:3) and (1:15), were irradiated by 40 MeV $^{58}Ni^{11+}$ ions. Fourier transform transmission spectroscopy in the mid-range was used to monitor the evolution ices at 15 K as a function of projectile fluence. New IR bands appearing for the irradiated (CH_4:H_2O) (1:3) ice are attributed to the synthesized molecules: C_3H_8, HCO, H_2CO, CO, CO_2, H_2O_2, HCOOH, CH_3OH, C_2H_5OH, and CH_3CHO. For the irradiated (CH_4:H_2O) (1:15) ice, the abundances of the compounds containing two carbons atoms are lower than those for the (1:3) ice; in contrast, CH_3OH and H_2O_2 abundances increase when compared to the values obtained with the (1:3) ice. After irradiation, the ices were warmed up until 110 K, when the IR spectra reveal features of complex organic molecules. The destruction and formation cross sections and the sputtering yields of the ice mixtures are estimated. These findings provide possible pathways for the occurrence of compounds rich in C, O, and H, which are indeed observed in the cold regions of the universe such as ices in grain mantles of the interstellar medium and circumstellar envelopes.

Unified Astronomy Thesaurus concepts: Astrochemistry (75); Interstellar molecules (849); Laboratory astrophysics (2004); Spectroscopy (1558); Surface ices (2117)

1. Introduction

The study of ices existing in the cold regions of the universe informs us about the evolution of their chemical and physical properties triggered by energetic processes, including cosmic radiation (i.e., photons and energetic particles). Water and methane molecules in solid phases are common in the coldest zones of the solar system (SS; see Gudipati & Castillo-Rogez 2013, and references therein). Water ices containing methane have also been observed in comets (Mumma & Charnley 2011, and references therein). Far away from the SS, solid methane coexists with other organic molecules, e.g., H_2O, CO, CO_2, NH_3, and CH_3OH (Dartois 2005). The methane in the solid phase was observed in different interstellar environments of the colder regions of low, intermediate, and high massive young stellar objects (LYSOs, IYSOs, and MYSOs), quiescent regions, and in the center and external galaxies, as can be seen in Figure 1. These observations were made using space-based observatory facilities that provide infrared (IR) light spectra data. The solid methane percentages relative to solid water were reported by numerous studies that are briefly reviewed in the paragraphs that follow.

Methane molecules have been identified in the gas and solid phases at 1304 cm^{-1} (7.67 μm), by Lacy et al. (1991) and Boogert et al. (1996, 1997, 1998), which were in the dense molecular clouds of the MYSO: W33 A, NGC 7538: IRS 1, and NGC 7538: IRS 9 at solid phase concentrations of CH_4 of approximately 0.3%, 3%, and 1.2% of the water ice column density (N_{H_2O}), respectively. The gas/solid ratio of CH_4 varies from 0.3 to 0.7 in these massive protostar. Dartois et al. (1998) found solid methane with $CH_4 \sim 3.9\% N_{H_2O}$ and a gas/solid ratio of 0.28 of the observation spectrum from HYSO RAFGL 7009S. Boogert et al. (2004a) identified the features 3012 cm^{-1} (3.32 μm) and 1300 cm^{-1} (7.7 μm) in the spectrum of NGC 7538 IRS 9 (Figure 1(b)) with a gas/solid ratio of 0.23. Solid CH_4 was observed in MYSO by d'Hendecourt et al. (1996) with $CH_4 \sim 4\%$ N_{H_2O}, from observation of the protostellar object RAFGL 7009S, and also by Gibb et al. (2000) with $CH_4 \sim 1.55\%$ N_{H_2O}, measured from the spectrum source of the W33A object.

The existence of solid CH_4 in the envelopes and disks of LYSOs was reported by several studies, as follows: White et al. (2000) with $CH_4 \sim 1\%$ N_{H_2O} in the star formation regions of L1551 IRS 5 and L1551 NE; Gürtler et al. (2002) with 1%–2% in five sources in cold and dense molecular circumstellar envelopes of Barnard 5, W33A, HH 100—IRS, Cep A, NGC 7538:IR9, W3:IRS5, and AFGL 2591; Alexander et al. (2003) in the circumstellar environment of the clouds RCrA, ρ Ophiuchi, Serpens, and Chamaeleon I; Noriega-Crespo et al. (2004) with 2% in HH 46 IRS 1 and HH 47A; Boogert et al. (2004b) in embedded protostars B5 IRS1 and HH 46 IRS1; Boogert et al. (2004a) in NGC 7538 IRS 9 (Figure 1(b)); and Öberg et al. (2008) from 2% to 13% in 25 of out 52 ice sources in the Cores to Disks (c2d). In the external galactic nucleus (Figure 1(c)), Spoon et al. (2001) detected CH_4 with 2% in the ice on the enshrouded AGN of NGC 4418.

In the Galactic center, Chiar et al. (2000, 2002) studied the composition and distribution of dust along the line of sight toward Sgr A* GCS 3 and GCS 4 with less than 5% (Figure 1(a)). Gibb et al. (2004) analyzed 23 IR sources that were taken from young stellar objects (LYSO, IYSO, and MYSO), quiescent dark clouds, and the diffuse interstellar medium; solid CH_4 was detected in 17 of them with proportions from 1.3% to 17%. In the quiescent interstellar medium, Knez et al. (2005) found <3% in the clouds. While Zasowski et al. (2009) calculated $CH_4 \sim 3\%$ in LYSO,

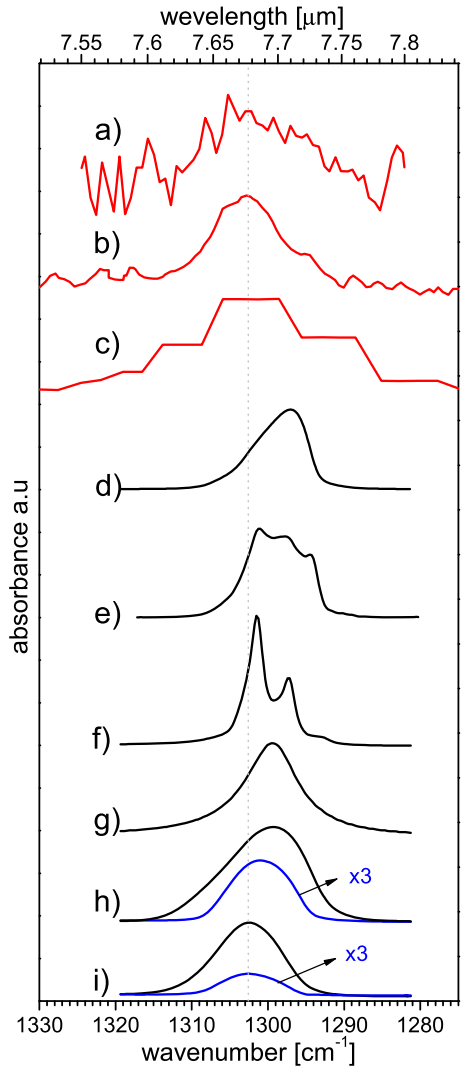

Figure 1. IR feature ν_4 of interstellar solid CH_4 is shown in panels (a)–(c). Panel (a): $CH_4 \sim 2\%$ N_{H_2O} toward Sagittarius A* source in the galactic center (Chiar et al. 2000); panel (b): $CH_4 \sim 1.3\%$ N_{H_2O} toward HYSO source of NGC 7538 IRS 9 (Boogert et al. 2004a); panel (c): $CH_4 \sim 5.3\%$ N_{H_2O} in LYSO source of B1-c (Öberg et al. 2008). Pure CH_4 ices are shown in panels (d)–(g). Panel (d): amorphous at 10 K (Gerakines & Hudson 2015); panel (e): combined amorphous and phase II at 15 K (Mejía et al. 2013); panel (f): phase II at 10 K (Gerakines & Hudson 2015); panel (g): phase I at 35 K (Mejía 2013). In panels (h) and (i), spectra correspond to the (1:3) and (1:15) ices, respectively; the spectra acquired before (black line) and after (blue line) irradiation (at 10^{13} ions cm^{-2}) are shown. For ease of comparison, data of irradiated ices have been multiplied by three.

Boogert et al. (2011) studied the proportion of CH_4 behind isolated dense cores of 31 stars with values <23%. Öberg et al. (2011) studied the ices in cloud cores of LYSO and MYSO; the solid CH_4 abundance was about 5% in these environments.

The CH_4 molecule is likely formed on grain surfaces by hydrogenation of C atoms (Gibb et al. 2000). After that, the CH_4 may evaporate by temperature increase; this might explain the CH_4 gas/solid rate from 0.28 to 0.7 in the cold regions of interstellar objects (Gibb et al. 2004). Graninger et al. (2016) argued that carbon chains detected in protostars were likely desorbed from the icy mantle; their findings suggest a similar origin for the observed gaseous molecules. In contrast with Graninger et al. (2016), Bergantini et al. (2017) detected a variety of complex organic molecules (COMs) in CH_4:H_2O ices irradiated by 5 keV electrons. These findings indicate a need to understand the chemical synthesis triggered by different types of ionizing radiation as well as the link between the physical processes with the chemical processes during the irradiation of solid phase compounds.

The ices in the outer SS are exposed constantly to solar radiation and galactic cosmic-rays (Bennett et al. 2013, and references therein), while galactic cosmic-rays bombard the ices of ISM and circumstellar envelopes (van Dishoeck et al. 2013, 2014). The chemical and physical processes studied in this paper are: (i) chemical changes in the ice bulk leading to the synthesis of new compounds, and, (ii) desorption of neutral and charged species. The physico-chemical effects of CH_4:H_2O ice radiolysis by energetic ion bombardment are studied. The CH_4:H_2O mixture was chosen to mimic the observed proportion (from 0.3% to 17%) in the icy mantles (Gibb et al. 2004). The findings are expected to bring relevant insights into the evolution of astrophysical ices irradiated by swift heavy cosmic-rays. In the next section, after presenting a literature review, the relevance of energetic heavy ions on the radiolysis of astrophysical ices will be discussed.

1.1. Previous Studies on CH_4:H_2O Ices

The following paragraphs present a short review of previous experimental methane-water ice radiolysis studies using photon, electron, and ion beams.

The ultraviolet (UV) photolysis (8.4–10 eV) of methane clathrate (CH_4:5.75 H_2O) at 77 K was studied by Stief et al. (1965); the molecules H_2, CO, CO_2, and C_2H_6 were detected. Cottin et al. (2003) performed a similar experiment (with UV 7.4 eV) to show that the photodestruction of CH_4 in the ice mixture (CH_4:H_2O) (1:10) ($T < 20$ K) was more effective than that in the irradiated pure CH_4 ice; the formation of new compounds was not analyzed in their work. In an analysis of photoproducts after UV irradiation (from 3.7 to 9.5 eV) of CH_4:H_2O (1:9) ice ($T = 20$ K), Hodyss et al. (2009) found CO, CO_2, H_2CO, CH_3OH, and C_2H_6; their molecular abundances were such that $CH_3OH > H_2CO \approx CO > CO_2$.

The changes in the abundance of synthesized products: CO, C_2H_6, C_2H_4, H_2CO, CH_3OH, CH_3CHO, and CH_3CH_2OH were analyzed by Öberg et al. (2010) in order to better understand the photolysis of (CH_4:H_2O) ices (1:x, where x = 0.3, 1, 2, 3, 4, and 5) and its effects at different temperatures. The explanation proposed for the relative abundance of the produced molecules, at different H_2O concentrations, was that the dissociation of CH_4 and H_2O forms radical molecules, i.e., CH_2, CH_3, and OH, and these depend on radical diffusion to react chemically. With respect to the effects of the irradiated sample temperature (at 20 and 60 K), no link was found with the product abundances. In contrast, new molecules were distinguished during the slow warming up from 20 to 70 K.

Recently, Suhasaria et al. (2018) used pulses of 40.8 eV photons to induce desorption from CH_4:D_2O (1:3.3) ice; a quadrupole mass spectrometer was employed for identifying the following desorbed species: H_n^+, D_n^+, CH_n^+, $C_2H_n^+$, $C_3H_n^+$, O_2^+, CO^+, CO_2^+, H_2CO^+, CH_3CHO^+, and series of C_n^+ clusters (with n up to 12).

Thompson et al. (1987) studied radiolysis by coronal discharges (electron beams), and darkening of the sample was observed. After irradiation, the residue was analyzed by both UV-visible and IR transmission spectroscopy; the spectra revealed molecular bonds corresponding to alkanes, alkenes, and aldehydes. Wada et al. (2006) used electron beams

(10–300 eV) to analyze the CH_3OH synthesis from (CH_4:H_2O) (1:10) ice (at 10 K), irradiated at different ice thicknesses and electron fluxes. The products identified in the IR spectrum were H_2CO, C_2H_6, C_2H_4, and C_2H_2; these molecules were also detected (after irradiation) by thermal desorption spectrometry (TDS). In a recent study, Bergantini et al. (2017) irradiated CH_4:H_2O (1:9) ice with 5 keV electrons; during irradiation, C_2H_6, CH_3OH, and CO_2 were detected. TDS analysis (after irradiation) identified C_2H_5OH and CH_3OCH_3 and suggested the formation of CH_3CCH, H_2CCO, CH_2CHCH_3, CH_2CHOH, CH_3CHO, and CH_3OOH.

Ion irradiation experiments with protons (1 MeV) were performed by Moore (1981); the synthesized molecules observed in the IR spectrum, after the irradiation of CH_4:H_2O (2:5) ice ($T < 20$ K), were CO, CO_2, and C_2H_6. Moore & Hudson (1998) repeated the experiment but irradiated CH_4:H_2O (1:x; where $x = 2$, 7, and 15) ice films (at $T < 20$ K) with 0.8 MeV H^+ up to 17 eV molec^{-1} dose. They identified the following molecular species: C_3H_8, CH_3OH, C_2H_5OH, CO, CO_2, CH_3CHO, and H_2CO. The abundances of these molecules show a dependence on the H_2O concentration in the CH_4:H_2O mixture (see Moore & Hudson 1998, Table 2).

The CO_2 formation and the spectral characteristics of its band 2340 cm^{-1} were studied by Palumbo et al. (1998) performing He^+ (3 and 30 keV) ion bombardment of CH_4:H_2O (1:2 and 1:1) ices. Finally, Garozzo et al. (2011) used He^+ (30 keV) to irradiate CH_4:H_2O (1:4) at different temperatures (12 and 40 K). They found that the CH_4 molecules are more efficiently destroyed at 40 K than at 12 K. With regard to the synthesized species, CH_3OH, C_2H_6, CO_2, CO, and H_2CO were detected.

Although chemical changes have been studied independently with incident UV photons, electrons, and light ions (i.e., H^+ and He^+), the destruction and formation yields have not been treated in a comprehensive way. Recent results show that the destruction cross sections obtained by swift heavy ions are vastly higher than those produced by light ions or electrons (Seperuelo Duarte et al. 2010; de Barros et al. 2011a). On the other hand, in spite of heavy ion abundances in the solar wind and in cosmic-rays being a significant percentage lower than that of light ions, the deposited energy rates by projectile are usually much higher; e.g., for H and Fe ions with energies from 10 to 10^3 MeV nucleon^{-1}, the ratios of their deposited energy rates (Fe/H) by electronic interaction vary from 10 to 10^3 (see Mejía et al. 2013, their Figure 10).

The main goal of this work is to monitor the production of new molecular species as a consequence of CH_4:H_2O radiolysis by swift heavy ions. The destruction and formation cross sections of observed compounds and the sputtering yield of the ice are measured as well.

2. Experimental

The experiments in this study were carried out at the heavy ion accelerator facility, Grand Accélérateur National d'Ions Lourds, Caen—France (GANIL; Seperuelo Duarte et al. 2009). The experimental setup consists of a high vacuum chamber with a base pressure of 3×10^{-7} mbar at room temperature, while at 15 K, it can reach about 10^{-8} mbar. The vacuum chamber is coupled with a closed-cycle helium cryostat finger that holds a CsI substrate; this finger can reach a minimum temperature of 15 K. Connected to the substrate is a heater system that allows us to increase the temperature with selectable ramps up to 300 K. A previous run, "blank experiment—type" has been performed with the same system and without gas deposition (Mejía 2013). A clean CsI substrate, at 15 K, was kept for 6 hr inside the vacuum chamber at 10^{-8} mbar; FTIR analysis showed that H_2O molecules from the residual gas became stuck over the two sides of the CsI substrate with a rate of 8×10^{14} molec h^{-1} cm^{-2}. Assuming the same condensation rate, less than 2.5×10^{15} molec h^{-1} cm^{-2} of H2O would condense over the substrate during the same time of the irradiation experiment. Actually, during the CH_4:H_2O experiment, the condensation rate is expected to be higher because H_2O vapor was injected into the chamber, favoring adsorption in the walls. As a result, the H_2O cross-section measurement should be considered with caution.

A gas mixing chamber (base pressure of 10^{-6} mbar) is connected to the vacuum chamber. The H_2O vapor at 15 mbar was mixed with CH_4 in an adequate partial pressure and then injected onto the cold IR transparent window via a thin tube. The ultra pure liquid water has an electric conductivity of 10^7 Ω cm (Milli-Q), and the purity of the methane gas is 99.995% (Messer Griesheim). To make the deposition onto the CsI substrate (at 15 K), the finger was turned so that the substrate faces the injection tube (4 mm diameter); the distance between the tube and the CsI substrate is ∼10 mm. After that, a valve was opened to deposit the gas mixture onto the substrate for nearly 3 minutes for the (1:3) ice, and 2 minutes for the (1:15) ice. During the gas deposition, the pressure in the main chamber rose up to 10^{-7} mbar. The deposition rate was estimated as nearly 10 ± 2 nm s^{-1}, producing ice films of a few micrometers thick.

The main chamber is connected to the beam line IRRSUD for heavy ion irradiation by 40 MeV $^{58}Ni^{11+}$ (E/m∼ 0.69 MeV nucleon^{-1}) with constant flux (10^9 ion cm^{-2} s^{-1}). The $^{58}Ni^{11+}$ ion beam was chosen for the nickel and iron relative abundance of around 2.2×10^{-4} with respect to hydrogen in the galactic cosmic-ray distribution (Tanabashi et al. 2018). The average radiolysis effects of heavy ions can be as far as 10^3 times higher than those of protons at the same velocity and with the same flux (de Barros et al. 2011a; Mejía et al. 2013). The ion bombardment was performed at normal incidence on the CH_4:H_2O ice films. At fluences of 0.01, 0.03, 0.06, 0.1, 0.3, 0.6, 1, 3, 6, and 10×10^{12} ion cm^{-2}, irradiation was stopped for acquiring FTIR spectra. The exposure to swift heavy ion bombardment lasted 170 minutes long for both samples. After irradiation of the (1:3) ice, a temperature increase was performed from 15 to 110 K with a ramp at ∼0.5 K minute^{-1}; at 110 K, the most volatile species had sublimated, and the procedure was stopped. Spectra were recorded every 10 K; recording each IR spectrum took around 2 minutes. Mass spectrometry and FTIR spectroscopy are powerful and complementary techniques for identifying molecules: the former determines the mass/charge of ions formed after an excitation of the sample molecules; the latter is capable of identifying vibrational modes of the chemical bonds in a molecule and their functional groups. It is worth mentioning that the detection of several bands provides good confidence in vibrational mode identification.

In Table 1, the ion-solid interaction parameters are shown; the SRIM code (Ziegler et al. 2010) was used to calculate the corresponding stopping powers. Partial contributions of the CH_4 and H_2O molecules are also presented; the total stopping power takes the molecular stoichiometry and ice concentrations

Table 1
Initial Column Densities, N_0, and Electronic and Nuclear Stopping Powers, S_e and S_n, for the Nickel Projectile in (CH_4:H_2O) Ices

	(1:3) Ice			(1:15) Ice		
Parameter	CH_4	H_2O	Total	CH_4	H_2O	Total
N_0[a] (10^{18} molec cm^{-2})	1.2 ± 0.4	3.6 ± 0.5	4.8	0.20 ± 0.06	3.0 ± 0.4	3.2
S_e[b] (10^{-15} eV cm^2 molec^{-1})	550	1000	1550	150	1330	1480
S_n[b] (10^{-15} eV cm^2 molec^{-1})	1.9	3.4	5.3	0.52	4.65	5.17

Notes. Individual contributions of CH_4 and H_2O are also displayed.
[a] Deduced from the Lambert–Beer law, $N = 2.30(\text{integratedabsorbance})/\mathcal{A}_v$.
[b] Obtained from Ziegler et al. (2010) with 10%–15% of error.

into account. The penetration depths of 40 MeV $^{58}Ni^{11+}$ projectiles in the ice films are around 32 μm for (1:3) ice and 34 μm for (1:15) ice, with lengths much larger than the sample thickness. Therefore, cross sections can be considered constant along the track, since the projectiles traversed the ice film with approximately constant velocity and stopping power. The deposited dose is calculated by $D_i = S_e \times F_i$, where S_e is the electronic stopping power, and F_i is the fluence for irradiation i. The final doses achieved were around 15.5 and 14.8 eV molec^{-1} for the (1:3) and (1:15) ices, respectively. These doses are compared with those of the interaction of cosmic-rays with icy grains of the ISM, where the mean doses rate deposited in the ice mantles is around 6×10^{-15} eV molec^{-1} s^{-1} (Shen et al. 2004). Considering the equivalent timescale, the dose of 15 eV molec^{-1} corresponds to 80 million years.

After each irradiation, the sample was perpendicularly oriented toward the IR spectrometer (Nicolet Magna 550) for taking spectra in transmission mode. Each IR spectrum was collected by 128 scans from 5000 to 600 cm^{-1} (2–16.7 μm) with a resolution of 1 cm^{-1}. The Lambert–Beer law was employed: the column densities were obtained by dividing the band area by the A-value times 2.3.

A-values may depend on the initial ice structure, which affects the IR absorption by about 10% for H_2O (Palumbo 2006) and about 33% for CH_4 (Gerakines & Hudson 2015). According to Mejía et al. (2015b), the A-values of the precursor molecules may vary as the irradiation proceeds and the concentrations of the ice constituents change.

To calculate column densities, appropriate bands were chosen. They are: (i) for CH_4, the one at 4200 cm^{-1} whose A-value is $A_v = 3.6 \times 10^{-19}$ cm molec^{-1} (Brunetto et al. 2008; de Barros et al. 2011a), and (ii) for H_2O, the one at 3250 cm^{-1}, the value $A_v = 2.0 \times 10^{-16}$ cm molec^{-1}, reported by Allamandola et al. (1988) and Hagen et al. (1981) for pure H_2O at 10 K has been used. Their initial column densities, N_0, for the (CH_4:H_2O) ices are listed in Table 1. Errors are estimated to be 25%, considering typical A-value accuracies and the fact that the ice structure is not controlled. The thicknesses (ℓ_0), about 1.82 μm (for (1:3) ice) and 1.07 μm (for (1:15) ice), were calculated from $\ell_0 = (mN\rho)_{CH_4} + (mN\rho)_{H_2O}$, where N is the column density (in molec cm^{-2}), m is the molecular weight, and ρ is the density in the solid phase for CH_4 and H_2O molecules, respectively. These density values were taken from Bossa et al. (2015). In the current work, two samples (CH_4:H_2O), at concentrations of (1:3) and (1:15), at 15 K were irradiated by 40 MeV $^{58}Ni^{11+}$ ion beam, corresponding to $E/m \sim 0.69$ MeV nucleon^{-1}.

3. Results

The observed changes in the IR spectrum caused by swift heavy bombardment 40 MeV $^{58}Ni^{11+}$ on CH_4:H_2O ice are shown in Figure 2; they are similar to those reported by Moore & Hudson (1998), Wada et al. (2006), Hodyss et al. (2009), Öberg et al. (2010), and Garozzo et al. (2011). Relevant sections of the CH_4 IR spectra acquired before and after irradiation are compared in Figure 3. The modifications in the IR spectra caused by ionizing radiation on (CH_4:H_2O) (1:3) and (1:15) ices, as well as those due to annealing effects after irradiation, are described in the sections that follow.

3.1. Ice Structure

The amorphous structure of CH_4 pure ice is identified by the presence of the fundamental bands ν_1 (2904 cm^{-1}) and ν_2 (1530 cm^{-1}; Mejía et al. 2013; Hudson et al. 2015). Figure 3 shows that the ν_1 and ν_2 bands are present during irradiation, and Figure 1 illustrates the IR spectrum profiles of the ν_4 band at different ice structures and water concentrations as well. Gerakines & Hudson (2015) have demonstrated that the spectrum of Figure 1(d) corresponds to amorphous CH_4 ice, which presents profile differences when compared with the spectra of ices in phase II (Figure 1(f)) and in phase I (Figure 1(g)). For example, in Figure 1(d), the absence of the double peak feature and the asymmetric absorption band indicate an amorphous CH_4 ice. The spectrum in Figure 1(e) is interesting because it shows the effects of both structures: the amorphous ice (with ν_1 and ν_2 features) and the crystalline phase II (with three peaks; Mejía et al. 2013); nevertheless, the proportion of phase II is unknown. Correspondingly, the spectrum of Figure 1(h) depicts an amorphous CH_4:H_2O (1:3) ice, but its profile is more symmetric when compared with the one of pure amorphous CH_4 ice (Figure 1(d)). The asymmetric profile is almost lost in the spectrum of Figure 1(i); however, the (1:15) ice is mostly amorphous. The peak position of the ν_4 band is displaced toward the left side as the concentration water increases from 1297 cm^{-1} (pure CH_4) toward 1299 cm^{-1} (1:3) and to 1302 cm^{-1} (1:15) (Figures 1(h) and (i)).

The dangling bond features of H_2O are denoted in Figure 2 near 3684 and 3670 cm^{-1}. As Palumbo (2006) and Mejía et al. (2015b) pointed out, the dangling bonds are an indicator of porous amorphous water ice; furthermore, these bands disappear for doses above ~1 eV molec^{-1} when the porous ice becomes amorphous with a minimum porosity (Dartois et al. 2013). Together, these results indicate that the (CH_4:H_2O) ice structure, observed in Figures 1–3, corresponds to

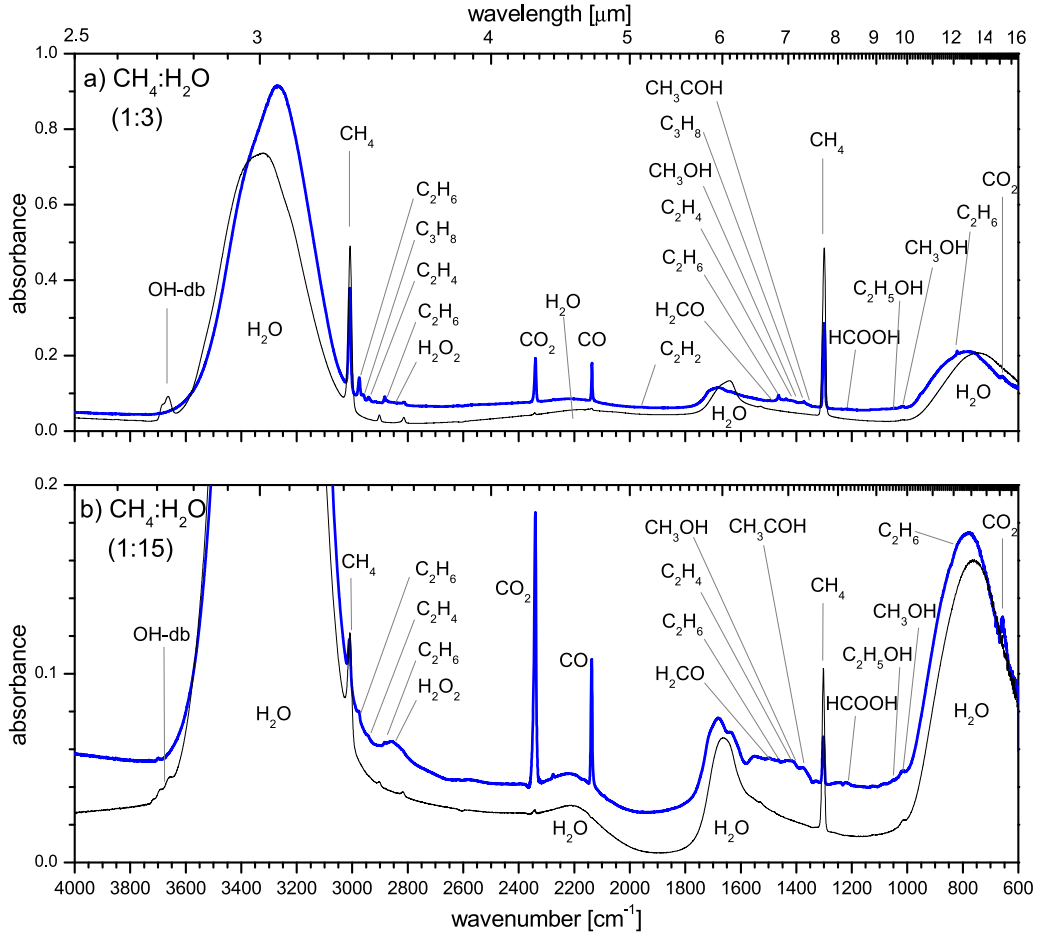

Figure 2. IR spectra of (CH_4:H_2O), for, panel (a), (1:3), and, panel (b), (1:15) ices mixtures, before irradiation (thin black line) and after irradiation (thick blue line) with 10^{13} ions cm^{-2} of 40 MeV $^{58}Ni^{11+}$. Each new IR band attribution is given in Table 2.

amorphous porous ice before irradiation, which then becomes gradually amorphous compacted ice during irradiation.

3.2. Spectroscopic Identification of the Molecules Synthesized by the Irradiation of CH_4:H_2O (1:3) Ice

Figure 3 compares IR spectrum segments of (CH_4:H_2O) ice (1:3) at 15 K, before and after irradiation by 40 MeV $^{58}Ni^{11+}$ ions at the fluence of 10^{13} ion cm^{-2}. Figures 4–7 present the IR bands corresponding to synthesized compounds at the fluence of 6×10^{12} ion cm^{-2}; at this fluence, the IR bands of some products and their column densities reach a maximum, as can be seen in Figures 8 and 9.

The new absorption bands are summarized in Table 2, which correspond to new molecular species that may be classified in terms of their families of organic compounds and functional groups as follows:

(i) Formyl radical, HCO; only this radical was detected.
(ii) *Hydrocarbons*: ethane C_2H_6, propane C_3H_8, acetylene C_2H_2, and ethene C_2H_4.
(iii) Peroxide hydrogen H_2O_2.
(iv) *Carbon oxides*: carbon dioxide CO_2, carbon monoxide CO, as well as their isotopic species $^{13}CO_2$ and ^{13}CO.
(v) *Aldehydes*: formaldehyde H_2CO and acetaldehyde CH_3CHO.
(vi) *Alcohols*: methanol CH_3OH, ethanol C_2H_5OH, and ethylene glycol $C_2H_4(OH)_2$.
(vii) *Acids*: formic acid HCOOH, and acetic acid CH_3COOH and *ester*: methyl formate $HCOOCH_3$.
(viii) Others: *ketone*—acetone $(CH_3)_2CO$, and *ether*—dimethyl ether $(CH_3)_2O$.

Figure 4(a) shows 14 spectra of (CH_4:H_2O) (1:3) and (1:15) from 1550 to 1350 cm^{-1} after irradiation with 6×10^{12} ions cm^{-2} (spectra 1 and 2); these spectra are compared with those of the ice before irradiation. The spectrum (3) of the irradiated pure CH_4 labeled as (CH_4:H_2O) (1:0), obtained by Mejía et al. (2013), was used as a reference for the band identification of compounds other than hydrocarbons. The IR wavenumbers listed in Table 2 were used for the identification of synthesized molecules. For illustrative purposes, the non-irradiated IR spectra of H_2O ice mixtures (from 4 to 14), obtained from the database website (Hudson et al. 2019)[5], were included to clarify the observation of the new features of synthesized molecules. When these spectra are compared with those of irradiated CH_4:H_2O ices, the new features confirm the synthesized compounds.

As can be seen from Figure 4(a) (1530–1340 cm^{-1}), the molecular species for the observed peak wavenumbers have the followings candidates: formaldehyde, H_2CO, at 1496 cm^{-1} (de Barros et al. 2014a); ethene, C_2H_4, at 1436 cm^{-1} (Mejía et al. 2013); ethane, C_2H_6, at 1464 and 1370 cm^{-1} (de Barros et al. 2016); propane, C_3H_8 at 1465 cm^{-1} (Comeford & Gould 1961);

[5] http://science.gsfc.nasa.gov/691/cosmicice/spectra.html

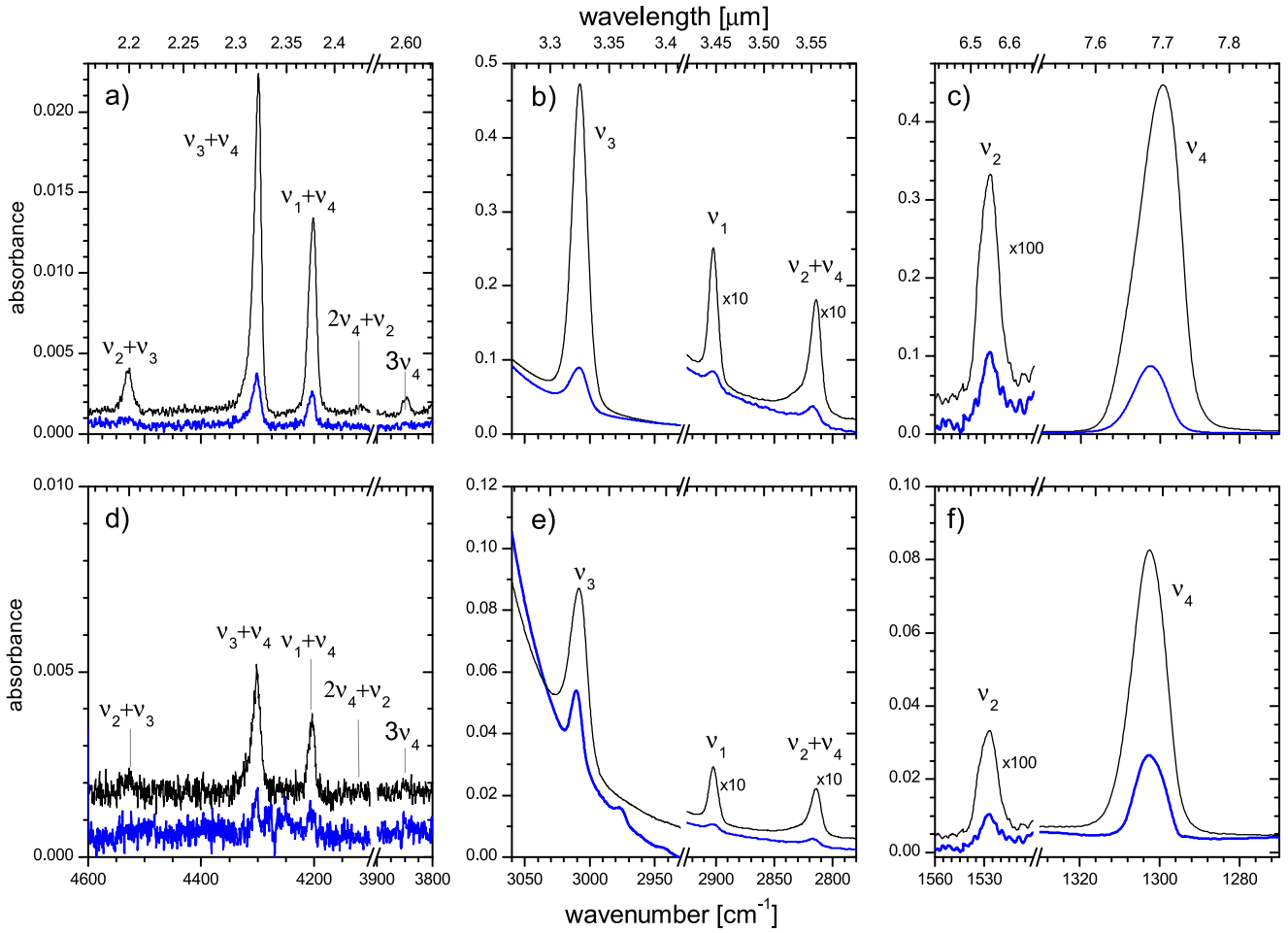

Figure 3. Selected segments of IR spectra of the main bands in the CH_4:H_2O ices at 15 K. Panels (a), (b), and (c) correspond to the (1:3) ice, and panels (d), (e), and (f) correspond to the (1:15) ice. Panels (a) and (d) are from 4600 to 3800 cm^{-1}; panels (b) and (e) are from 3060 to 2780 cm^{-1}; and panels (c) and (f) are from 1560 to 1270 cm^{-1}. The thin black lines represent the spectra acquired before irradiation; the thick blue lines correspond to sample after irradiation, with a fluence of 10^{13} ions cm^{-2}.

methanol, CH_3OH, at 1477, 1463, and 1450 cm^{-1} (Bennett et al. 2007; Öberg et al. 2009); acetaldehyde, CH_3CHO, at 1424 and 1350 cm^{-1} (Öberg et al. 2009); acetic acid, CH_3COOH, at 1422 and 1368 cm^{-1} (Rocha & Pilling 2014); ethanol, C_2H_5OH, at 1460, 1434, and 1384 cm^{-1} (Bennett & Kaiser 2007; Öberg et al. 2009); dimethyl ether, $(CH_3)_2O$ at 1477 and 1456 cm^{-1} (Bergantini et al. 2018); and acetone, $(CH_3)_2CO$, at 1443, 1424, 1372, and 1360 cm^{-1} (Andrade et al. 2014). As shown in Figure 4(a), the spectra of pure CH_4 ice before (4) and after irradiation (3) are used for better molecular identification (Mejía et al. 2013).

At the top of Figure 4(b) (spectra 15 and 16), two spectra are plotted in the range from 1280 to 990 cm^{-1} for (CH_4:H_2O) (1:3) and (1:15) ices, after irradiation fluence of 6×10^{12} ions cm^{-2}. Baseline subtraction was performed for better visualization of the absorption bands to both (1:3) and (1:15) ices (spectra 17 and 18); thus, the comparison of non-irradiated IR spectra of ice mixed with that of H_2O (spectra (19)–(25)) becomes easier (Hudson et al. 2019). In the region from 1280 to 1000 cm^{-1} (Figure 4(b)), the broad bands of formic acid, HCOOH, at 1220 cm^{-1} (Andrade et al. 2013) and methyl formate, $HCOOCH_3$, at 1230 cm^{-1} (Bennett & Kaiser 2007) overlap with each other, making it difficult to measure their column densities. Weak contributions due to acetone, $(CH_3)_2CO$, and methyl formate, $HCOOCH_3$, are observed at 1170 and 1160 cm^{-1}, respectively (Öberg et al. 2009; Andrade et al. 2014). The acetaldehyde, CH_3CHO, is easily identified by the 1130 cm^{-1} band (Öberg et al. 2009). The features in the region delimited between 1110 and 1030 cm^{-1} are attributed to the bands belonging to: ethanol (C_2H_5OH) at 1090 and 1044 cm^{-1} (Bennett & Kaiser 2007), acetone $(CH_3)_2CO$ at 1095 cm^{-1}, (Andrade et al. 2014), and ethylene glycol $C_2H_4(OH)_2$) at 1088 and 1045 cm^{-1} (Bennett & Kaiser 2007). The CH_3OH band is observed at 1026 cm^{-1} (Baratta et al. 1994). Together, these observations indicate that the molecules with isolated features are: H_2CO (1496 cm^{-1}), C_2H_5OH (1384 cm^{-1}), $(CH_3)_2CO$ (1160 cm^{-1}), CH_3CHO (1350 and 1125 cm^{-1}), and CH_3OH (1026 cm^{-1}).

The molecules present in the (1:3) and (1:15) ices are H_2CO, C_2H_5OH, CH_3CHO, and CH_3OH, whereas $(CH_3)_2CO$ is only observed in the (1:3) ice. By contrast, the candidate molecules that share the same features are: at 1460 cm^{-1}, C_2H_6, C_3H_8, CH_3OH, C_2H_5OH, and $(CH_3)_2O$; at 1430 cm^{-1}, C_2H_4, CH_3OH, CH_3CHO, CH_3OCOOH, C_2H_5OH, and $(CH_3)_2CO$; at 1370 cm^{-1}, the C_2H_4, C_3H_8, CH_3OH, CH_3OCOOH, C_2H_5OH, $(CH_3)_2O$, and $(CH_3)_2CO$; about the broad absorption band 1225 cm^{-1}, HCOOH and $HCOOCH_3$; around 1090 cm^{-1}, the candidates C_2H_5OH, $(CH_3)_2CO$, and $C_2H_4(OH)_2$; and, at 1050 cm^{-1}, the C_2H_5OH and $C_2H_4(OH)_2$ products.

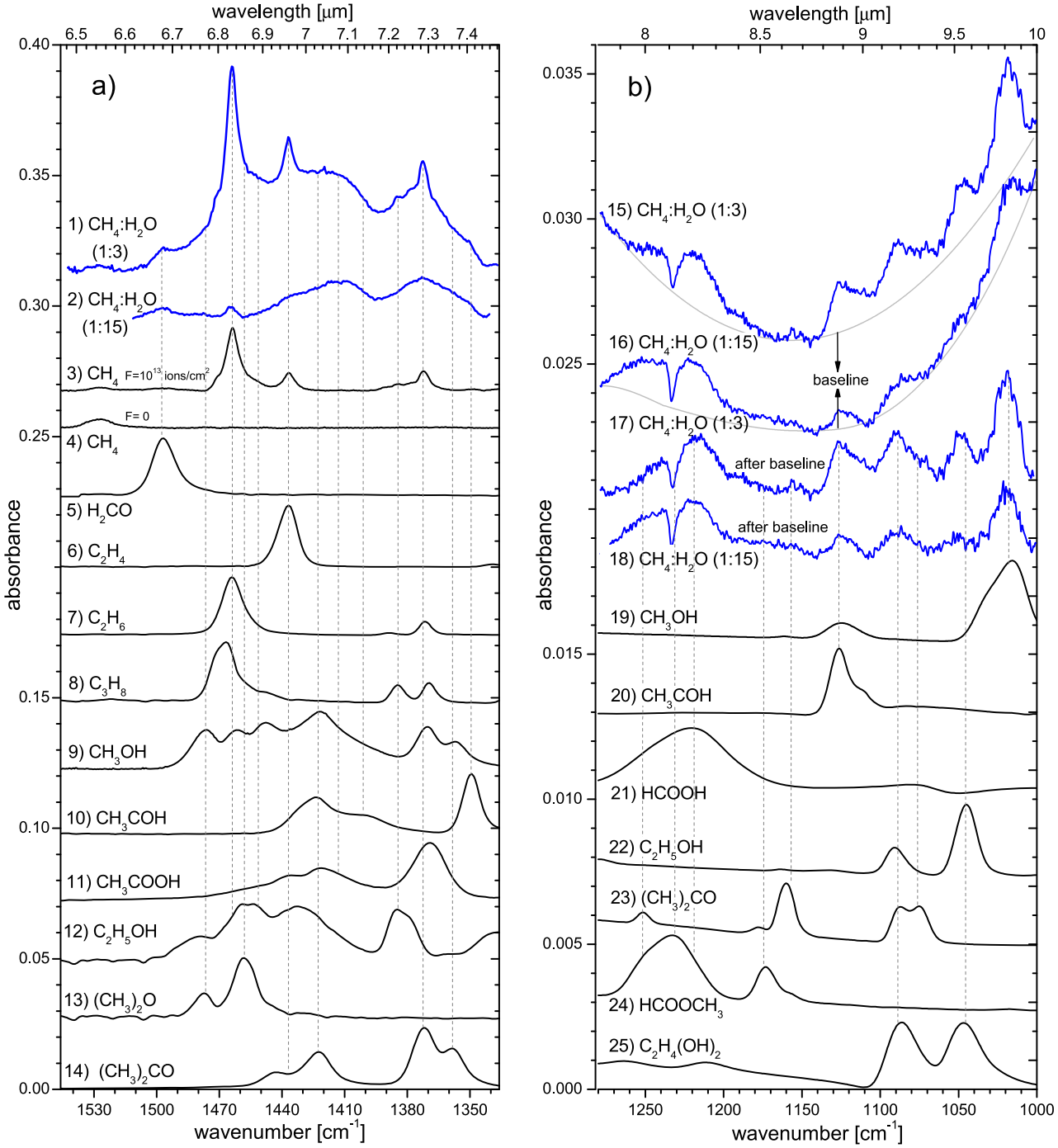

Figure 4. Panel (a) shows CH_4:H_2O IR spectra, from 1550 to 1350 cm^{-1}, for (1:3) and (1:15) concentrations, measured after irradiation, fluence: 6×10^{12} ions cm^{-2}. Additionally, the spectrum of pure CH_4 irradiated at the same fluence by 6 MeV oxygen ions is shown for comparison (Mejía et al. 2013). Panel (b) shows CH_4:H_2O spectra from 1280 to 990 cm^{-1}, for (1:3) and (1:15) concentrations measured after irradiation, fluence: 6×10^{12} ions cm^{-2}. A baseline was used to subtract the background and to obtain the third and fourth spectra. The other IR spectra correspond to non-irradiated X:H_2O ices mixtures, obtained from the database of Hudson et al. (2019) (http://science.gsfc.nasa.gov/691/cosmicice/spectra.html). The "X" in these X:H_2O ice mixtures at 15 K refers to the following molecular species and concentrations: (5) H_2CO (1:8), (6) C_2H_4 (1:20), (7) C_2H_6 (1:20), (8) C_3H_8 (1:22), (9) and (19) CH_3OH (1:5), (10) and (20) CH_3CHO (1:20), (11) CH_3COOH (1:10), (12) and (22) C_2H_5OH (1:20), (13) $(CH_3)_2O$ (1:20), (14) and (23) $(CH_3)_2CO$ (1:20), (21) HCOOH (1:9), (24) $HCOOCH_3$ (1:20), and (25) $C_2H_4(OH)_2$ (1:5). The vertical lines are references to guide the eyes.

Figure 5 presents, for the (1:3) and (1:5) mixtures, carbon monoxide (CO) and carbon dioxide (CO_2) absorption bands identified through the peaks 2134 cm^{-1} and 2343 cm^{-1}, respectively. The CO_2 line is also observed at 3600 and 3720 cm^{-1}. The isotopes ^{13}CO and $^{13}CO_2$ are detected via the 2092 and 2275 cm^{-1} lines; these compounds are often seen in experiments performed at laboratories by the same groups (Seperuelo Duarte et al. 2009, 2010; Mejía et al. 2013; de Barros et al. 2014a). The formyl radical HCO band is shown in Figure 5(d) at the position 1850 cm^{-1} (Bennett et al. 2007). Both molecules, CH_3COOH and HCO, are not observed in the spectra of the (1:15) ice during irradiation.

The wavenumber region depicted in Figure 6(a) presents some hydrocarbon lines, such as C_2H_6 (2975 cm^{-1}), C_2H_4

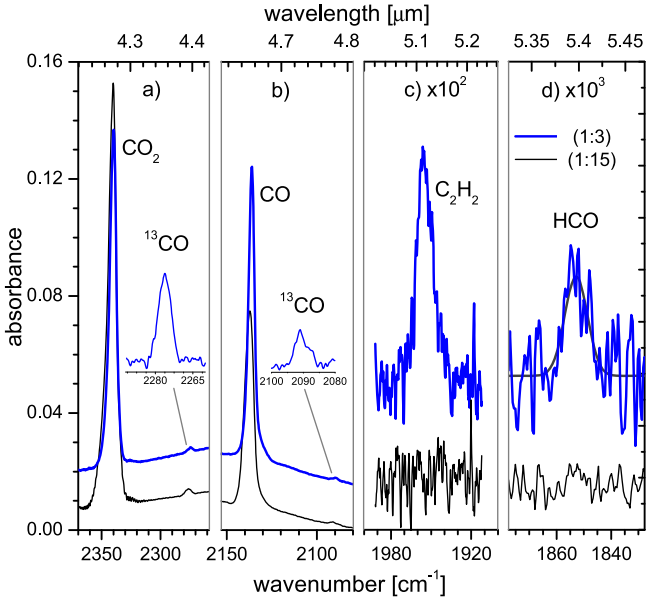

Figure 5. IR bands of synthesized products. Panel (a): ^{12}CO and ^{13}CO; panel (b): $^{12}CO_2$ and $^{13}CO_2$; panel (c): C_2H_2; and panel (d): HCO. The upper and lower lines correspond to irradiated (CH_4:H_2O) (1:3) and (1:15) ices, respectively, at fluence of 6×10^{12} ions cm^{-2}.

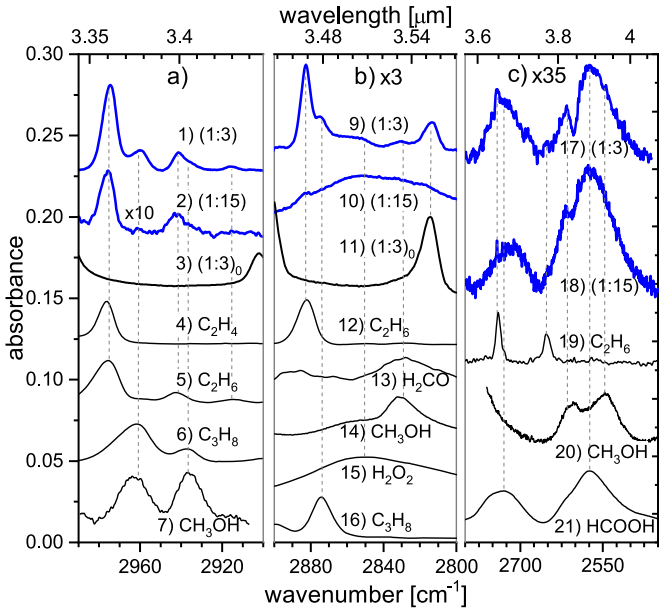

Figure 6. Identification of synthesized molecules produced by the radiolysis of (1:3) and (1:15) ices. Bands of irradiated (CH_4:H_2O) ice mixtures (6×10^{12} ions cm^{-2} fluence) are compared to bands obtained from non-irradiated pure ices. Panel (a) shows (2990–2900 cm^{-1}) corresponding to X:H_2O ices: (1) (CH_4:H_2O) (1:3) after irradiation (also 9 and 17), (2) (CH_4:H_2O) (1:15) after irradiation (also 10 and 18), (3) pure CH_4 non-irradiated (also 11), (4) C_2H_4:H_2O (1:20), (5) C_2H_6:H_2O (1:20), (6) C_3H_8:H_2O (1:22), and (7) CH_3OH:H_2O (1:5). Panel (b) shows (3000–2800 cm^{-1}): (12) C_2H_6:H_2O (1:20), (13) H_2CO:H_2O (1:8), (14) CH_3OH:H_2O (1:5), (15) H_2O_2:H_2O (3:100), and (16) C_3H_8:H_2O (1:22). Panel (c) shows (2800–2450 cm^{-1}): (19) C_2H_6:H_2O (1:20), (20) CH_3OH:H_2O (1:5), and (21) HCOOH:H_2O (1:9).

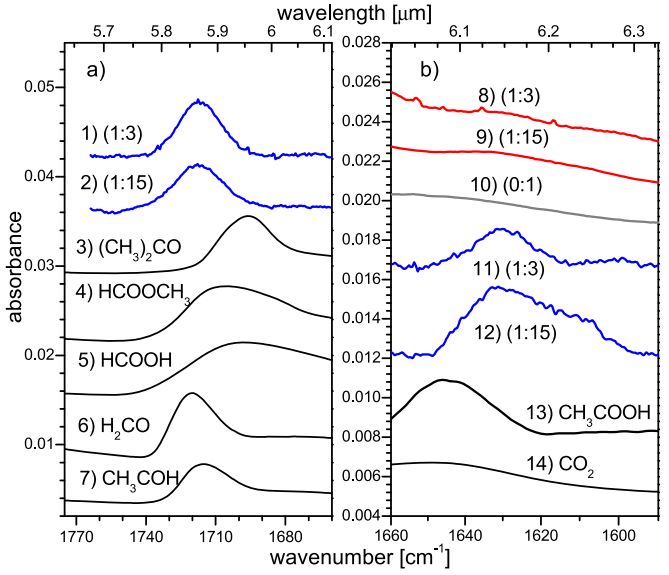

Figure 7. Irradiated ices (1, 2, 8, 9, 10, 11, and 12) exhibiting bands around 1720 and 1630 cm^{-1}, and the possible carriers of these bands (3, 4, 5, 6, 7, 13, and 14). Panel (a) shows spectrum (1) CH_4:H_2O (1:3) after irradiation; (2) CH_4:H_2O (1:15) after irradiation; (3) $(CH_3)_2CO$:H_2O (1:20); (4) $HCOOCH_3$:H_2O (1:20); (5) HCOOH:H_2O (1:9); (6) H_2CO:H_2O (1:8); and (7) CH_3CHO:H_2O (1:20). Panel (b) shows spectrum (8) CH_4:H_2O (1:3) after irradiation; (9) CH_4:H_2O (1:15) after irradiation; (10) H_2O after irradiation; (11) CH_4:H_2O (1:3) (after subtraction); (12) CH_4:H_2O (1:15) (after subtraction); and (13) CH_3COOH:H_2O (1:10); (14) CO_2:H_2O (1:10).

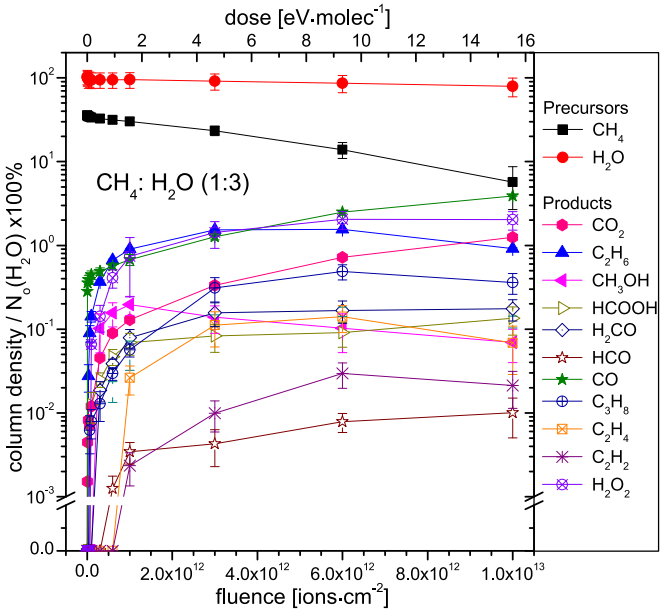

Figure 8. Evolution of normalized column densities (relative to N_{0,H_2O}) as a function of fluence for the (CH_4:H_2O) (1:3) ice irradiated at 15 K by $^{58}Ni^{11+}$. The CH_4 and H_2O abundances decreased while those of the synthesized products increased up to a maximum.

(2976 cm^{-1}), and C_2H_8 (2962 cm^{-1}; Mejía et al. 2013); moreover, a weak band of the CH_3OH (2961 and 2936 cm^{-1}) molecule is observed. The hydrocarbon peaks C_2H_6 (2882 cm^{-1}) and C_2H_8 (2874 cm^{-1}) are shown in Figure 6(b); the other contributions correspond to H_2CO (2830 cm^{-1}), CH_3OH (2827 cm^{-1}), and H_2O_2 (2848 cm^{-1}). Figure 6(c) exhibits a region where the broad HCOOH (2730 and 2575 cm^{-1}) bands dominate over two narrow peaks of C_2H_6 (2741 and 2650 cm^{-1}); a double band contribution due to the CH_3OH (2600 and 2530 cm^{-1}) is also seen. From the same figure, one sees that C_3H_8 is absent in the (1:15) ice spectrum.

Bands at 2800–2700 cm^{-1} characterize the C–H stretch; furthermore, strong and sharp absorptions in the 1720–1710 cm^{-1} region

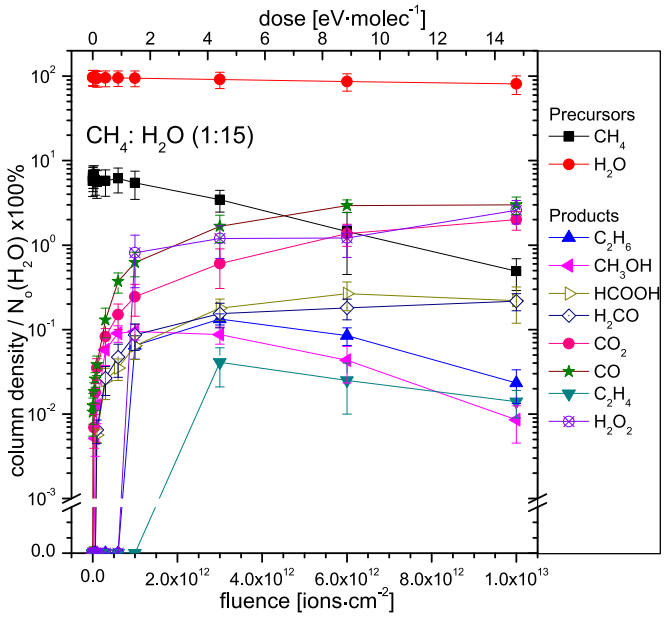

Figure 9. Evolution of normalized column densities (relative to N_{0,H_2O}) as a function of fluence for the (CH_4:H_2O) (1:15) ice irradiated at 15 K by $^{58}Ni^{11+}$. The evolutions of their synthesized products are also shown.

are usually produced by the highly polar C=O bond. Since the two bands are observed in the CH_4:H_2O irradiated ice spectra (Figures 6(b), (c) and 7(a)), small molecular species with both bonds are natural candidates to be products (Table 2), in particular, H_2CO (1720 cm^{-1}), CH_3COH (1720 cm^{-1}), $HCOOCH_3$ (1700 cm^{-1}), HCOOH (1700 cm^{-1}), and $(CH_3)_2CO$ (1695 cm^{-1}).

Formation of H_2CO is likely since its 1496 cm^{-1} band (Figure 4(a.5)) is also observed in CH_4:H_2O ices after irradiation; the same argument can be used for the formation of CH_3COH, which presents the observed 1350 and 1125 cm^{-1} bands (Figures 4(a.10) and (b.20)).

Formation of acetone $(CH_3)_2CO$ may also be claimed based on the observation of its 1180 and 1160 cm^{-1} bands (Figure 4(b.23)); however, its production should be lower because three carbon atoms are need for its synthesis (the other candidates have only one or two carbon atoms).

HCOOH (Figure 4(b.21)) and $HCOOCH_3$ molecules (Figure 4(b.24)) also exhibit other bands near those of CH_4:H_2O ice after irradiation; however, they are two oxygen molecules, and their 1700 cm^{-1} bands (Figure 7(a.5)) are not as sharp as those of the other candidates. In conclusion, all five molecular species are possibly formed, but H_2CO and CH_3COH should be favored by reaction mechanisms.

Relevant findings emerge from the comparison between results presented in Figures 8 and 9, as follows:

(i) The behavior of the H_2O radiolysis is basically the same for both ice mixtures, as expected for the most abundant precursor. Consistently, H_2O_2 is an abundant product, with a slightly higher production rate in the (1:15) ice mixture.

(ii) The lower CH_4 concentration is a result of its faster destruction: recombination is less likely. As a consequence, carbon-containing products are relatively more abundant in the poor-CH_4 ice mixture.

Table 2
Daughter Molecules Produced by Irradiation of (CH_4:H_2O) (1:3), Their Band Wavenumbers, Wavelengths, and *A*-values ($\times 10^{-18}$ cm molec^{-1})

Molecule	cm^{-1}	μm	$\mathcal{A}_v$
(i) HCO	1850	5.40	15[a]
(ii) *Hydrocarbons*			
C_2H_2	1955	5.11	1.4[b]
	750	13.3	14–20[c]
C_2H_4	3095	3.23	…
	2976	3.36	…
	1436	6.96	3.1[c]
	952	10.5	15[c]
C_2H_6	2975	3.36	14.8[c]
	2882	3.47	
	2741	3.65	
	1464	6.83	4.5[c]
	1376	7.27	
	821	12.14	1.9[c]
C_3H_8	2962	3.36	15.8[c]
	2874	3.8	…
	1465	6.83	…
(iii)*Peroxide*			
H_2O_2	4687	2.13	…
	2848	3.51	57[d]
(iv) *Carbon oxides*			
CO_2	3697	2.70	…
	2341	4.27	76[e]
	655	15.27	…
CO	2136	4.68	11[e]
(v) *Aldehydes*			
H_2CO	2885	3.47	…
	2830	3.53	28.2[a]
	1720	5.81	1.83[a]
	1496	6.68	3.9[f]
	1244	8.04	1[f]
CH_3CHO	2870	3.48	…
	1715	5.83	30[g]
	1424	7.02	3.6[g]
	1350	7.41	4.5[g]
	1125	8.89	4.3[g]
(vi) *Alcohols*			
CH_3OH	2961	3.38	0.11[h]
	2936	3.40	…
	2827	3.54	4.7[h]
	2600	3.85	…
	2530	3.95	…
	1477	6.77	…
	1463	6.84	9.1[h]
	1450	6.90	4.7
	1430	6.99	…
	1125	8.89	1.3[h]
	1026	9.75	18[a,h]
C_2H_5OH	2979	3.36	…
	1460	6.85	…
	1434	6.97	…
	1384	7.23	1.9[i]
	1337	7.48	…
	1090	9.17	0.7[a]
	1044	9.58	19[f]
$C_2H_4(OH)_2$	1454	6.88	…
	1430	6.99	…
	1088	9.19	0.07[a,h]
	1045	9.57	9.3[a]
(vii) *Acids*			

Table 2
(Continued)

Molecule	cm^{-1}	μm	$\mathcal{A}_v$
HCOOH	2730	3.66	⋯
	2575	3.88	7[i]
	1700	5.88	24[i]
	1220	8.20	15[g]
CH_3COOH	1646	6.08	⋯
	1422	7.03	⋯
	1368	7.31	⋯
	1295	7.72	⋯
(viii) *Others*			
$(CH_3)_2CO$	1443	6.93	⋯
	1424	7.02	4.5[j]
	1372	7.29	13[j]
	1360	7.35	⋯
	1245	8.03	⋯
	1160	8.62	⋯
	1095	9.13	0.17[j]
$HCOOCH_3$	1700	5.88	⋯
	1454	6.88	⋯
	1434	6.97	⋯
	1230	8.13	21[k]
	1170	8.55	⋯
$(CH_3)_2O$	2830	3.53	⋯
	1477	6.77	⋯
	1456	6.87	⋯
	1081	9.25	⋯

Notes. The column densities have been calculated using the bands highlighted in bold. The right column is the continuation of the left column.
[a] Bennett & Kaiser (2007).
[b] Abplanalp & Kaiser (2020).
[c] Mejía et al. (2013).
[d] Loeffler et al. (2006).
[e] Seperuelo Duarte et al. (2010).
[f] de Barros et al. (2014a).
[g] Bennett et al. (2005).
[h] de Barros et al. (2011).
[i] Öberg et al. (2009).
[j] Andrade et al. (2013).
[k] Hudson & Moore (1999).
[l] Andrade et al. (2014).
[m] Loeffler et al. (2006).

(iii) The most abundant products generated by the radiolysis of both ice mixtures are CO, H_2O_2, and CO_2. This means that all four CH bonds of CH_4 and the two CH bonds of H_2O were broken in order to form CO and CO_2. The free atomic oxygen may also react with H_2O to form H_2O_2.
(iv) CH_3OH is rapidly formed via the $CH_4 + H_2O \rightarrow CH_3OH + H_2$ reaction, but its radiolysis is also very efficient: its fast destruction is clear.
(v) Ice radiolysis generates atomic/ionic species, as well as OH and CH_n radicals, around the projectile's nuclear track. They react to synthesize C_2H_4, C_2H_6, HCOOH, H_2CO, and H_2O_2.

The region around the H_2O band at 1650 cm^{-1}, depicted in Figure 7(b) for (1:3) and (1:15) ices as spectra (8) and (9), is difficult to analyze due to the low peak/background ratio. Peaks are enhanced by subtracting an H_2O spectrum acquired with a similar dose and adequately normalized from these spectra. The H_2O spectrum (10), obtained by Mejía et al. (2015a) has been used for this treatment; results are presented as spectra 11 and 12 for the two ice mixtures. Similarly, spectra 1 and 2 in Figure 7(a) were obtained.

The region around the 1720 cm^{-1} band is characterized by the H_2CO band (1720 cm^{-1}) and CH_3CHO (1715 cm^{-1}). A third H_2CO band is observed at 1496 cm^{-1} (Figure 4(a.4)), and two CH_3CHO bands are seen at 1350 and 1125 cm^{-1} (Figures 4(a.10) and (b.20)).

Other molecules are also candidates to produce these bands, although their positions are redshifted; they include $(CH_3)_2CO$ (1695 cm^{-1}), $HCOOCH_3$ (1700 cm^{-1}), and HCOOH (1700 cm^{-1}). The 1630 cm^{-1} band and the small bands observed at 1610 and 1600 cm^{-1} remain unidentified. On the other hand, the CH_3COOH (1646 cm^{-1}) and CO_2 (1650 cm^{-1}) bands appear to be close to these IR absorptions. Wavenumber shifts and peak broadening are common when different molecular species coexist in the same matrix ice: such data must be interpreted with caution (Gálvez et al. 2009; Knez et al. 2012).

Briefly, the main identified features observed in the spectra of the irradiated (1:3) ice mixture are: HCO (1850 cm^{-1}), C_2H_2 (1955 cm^{-1}), C_2H_4 (952 cm^{-1}), C_2H_6 (821 cm^{-1}), C_3H_8 (2962 cm^{-1}), H_2O_2 (4687 cm^{-1}), CO_2 (2341 cm^{-1}), CO (2136 cm^{-1}), H_2CO (1496 cm^{-1}), CH_3OH (1026 cm^{-1}), and HCOOH (2730 cm^{-1}).

Figures 8 and 9 display the evolutions of the precursor's and product's column densities (percentages normalized to $N_0(H_2O)$) as a function of ion fluence. The top panels show the CH_4 and H_2O abundances, and the bottom panes show the column densities for the synthesized products, which are seen to increase up to a maximum.

3.3. Analysis of the Irradiated CH_4:H_2O (1:15) Ice

Figure 9 presents the column densities of the precursor molecules CH_4 and H_2O and of the synthesized molecules for the (1:15) ice mixture at 15 K, as a function of the projectile fluence. The HCO, C_2H_2, and C_3H_8 vibration bands are absent upon irradiation of the (1:15) ice, as shown in Figures 5(c), (d), and 6(a), respectively. It should be remarked that in Figure 9, the C_2H_4, C_2H_6, and CH_3OH column densities reach a maximum and gradually decrease during the last three fluence steps. The following concentration decreases are observed: C_2H_6 from 0.90% to 0.02%, C_2H_4 from 0.07% to 0.014%, CH_3OH from 0.07% to 0.008%, and CO_2 from 2.7% to 1.25%.

On the contrary, other molecular concentrations have increased: H_2CO, from 0.18% to 0.22%, and HCOOH, from 0.13% to 0.22%. The final H_2O_2 column density remained constant: 0.72 and 0.84 $\times 10^{17}$ molec cm^{-2} for the (1:3) and (1:15) ice experiments, respectively. Since the (1:3) ice has 20% more water molecules and produces 17% less H_2O_2 molecules than the (1:15) ice, the higher CH_4:H_2O concentration ratio actually decreases the H_2O_2 formation rate by offering more carbon atoms to capture atomic oxygen. Ethanol C_2H_5OH, dimethyl ether $(CH_3)_2O$, acetone $(CH_3)_2CO$, and methyl formate $HCOOCH_3$ appear to be good candidates for the IR bands presented in the Figures 4 and 7.

3.4. Sample Warming after Irradiation

The irradiation of the (1:3) ice with $^{58}Ni^{11+}$ was stopped at the fluence of 10^{13} ion cm^{-2}. The sample was then warmed from 15 to 110 K with a ramp of ~0.5 K $minute^{-1}$. Due to heat transfer during the warming, the actual ice temperature should be lower than that of the cryostat head, which is the value read and reported. The IR

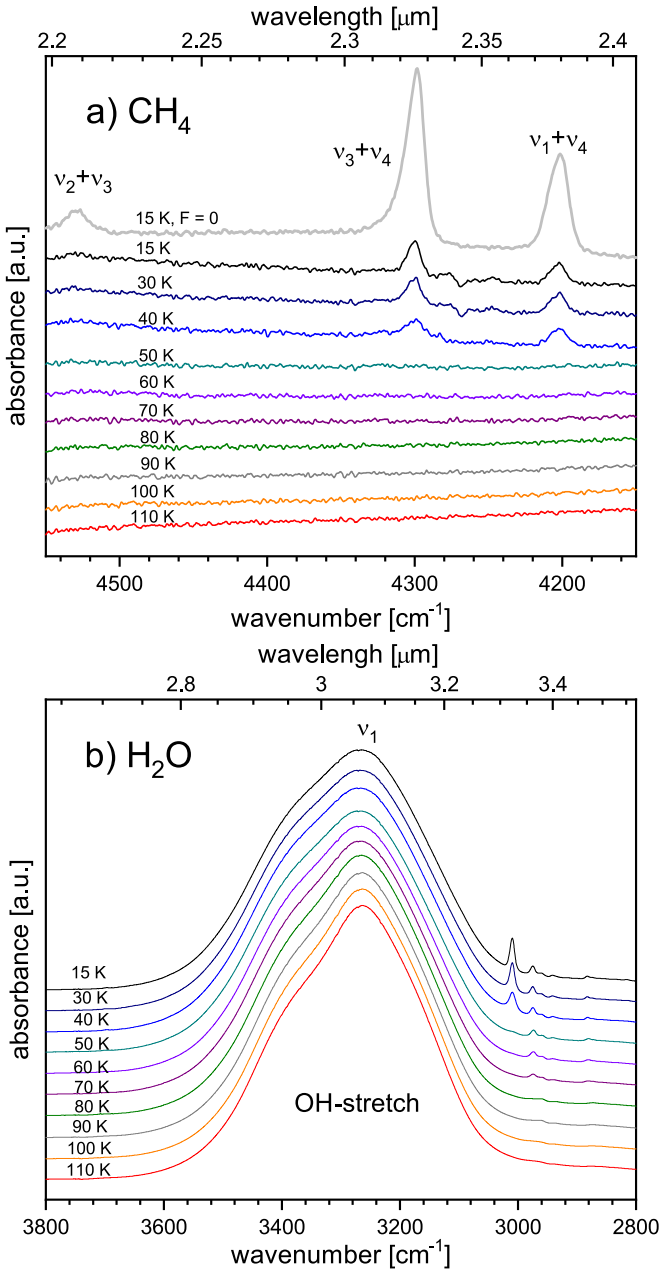

Figure 10. IR band evolution of irradiated (1:3) ice with increasing temperature. Panel (a): for CH_4 bands in the 4500–4150 cm^{-1} region; panel (b): for the H_2O absorption band.

spectrum evolution of CH_4 and H_2O, as the temperature increases, is illustrated in Figure 10. The bands of synthesized species are shown in Figures 11 and 12. In Figure 10, it can be seen that the CH_4 IR bands decrease at 40 K and disappear entirely at 50 K, due to degassing caused by sublimation (Gerakines & Hudson 2015). The H_2O IR feature becomes slightly narrower as the temperature increases and shows a profile similar to that obtained for amorphous ice (Dartois et al. 2015). Regarding the synthesized species, the observed changes in the IR band features (see Figures 11 and 12), as temperature increases, can be summarized as follows:

(i) At 30 K, the HCO band absorbance diminishes.
(ii) *Hydrocarbons*: all C_2H_6 band absorbances diminish after 60 K and disappear at 80 K. Those of the C_2H_4 bands disappear after 70 K. Those of the C_2H_2 and C_3H_8 decrease slowly up to 110 K.
(iii) The H_2O_2 band absorbance shows a small decrease at 70 K.
(iv) *Carbon oxides*: CO_2 (and $^{13}CO_2$) band absorbances decrease slowly up to 80 K, then decrease faster starting at 80 K; those of the CO and ^{13}CO bands almost disappear completely after 40 K. The CO column density decreases abruptly at 40 K, about 10 K above the sublimation temperature of pure CO ice (i.e., 30 K, Ponciano et al. 2006).
(v) *Aldehydes*: the H_2CO and CH_3CHO peaks remain constant during warming.
(vi) *Alcohols*: the CH_3OH and C_2H_5OH band absorbances as well as that of the candidate $C_2H_4(OH)_2$ do not exhibit any change.
(vii) *Acids*: the peaks of HCOOH and that of candidate CH_3COOH remain unaltered.
(viii) *Other molecules*: all possible candidates for the IR features, $(CH_3)_2CO$, $HCOOCH_3$, and $(CH_3)_2O$ remain stable during warming until 110 K.

The evolution of the column densities of the CH_4 and H_2O precursors and those of the some synthesized compounds, with increasing temperature, is displayed in Figure 13. The column densities are expected to decrease for all molecular species. The disappearance of some of the observed species is related to the observed by Öberg et al. (2009) and Bennett et al. (2010). The hydrocarbon's sublimation temperatures coincide with those measured by Bennett et al. (2006). The H_2O_2 column density stays constant until 110 K (Loeffler et al. 2006a). Carbon oxide's behavior coincides with the observations by Jamieson et al. (2006) and Bennett et al. (2009). Aldehyde's and alcohol's bands remain unchanged, and Öberg et al. (2009, 2010) and Bennett et al. (2010) observed the same unaltered behavior in the acid's features under warming. The column density behaviors of the other molecules do not vary as noted by Öberg et al. (2009). Finally, the identified band in Figure 11(h) does not display any absorbance change.

3.5. Cross Section and Sputtering Yield Measurement

Ionizing radiation leads to the fragmentation (dissociation) of molecules of the virgin sample (precursors). In turn, this process triggers chemical reactions between the fragment radicals, finally leading to the synthesis of new molecules. Furthermore, particles are ejected from the ice surface (sputtering). Radiolysis and sputtering occur simultaneously during the irradiation of the sample. Cross sections (for destruction/disappearance of precursors, as well as the formation of products, σ_d and σ_f, respectively) and total sputtering yields (Y_0) can be determined from the absorbance dependence on fluence of the distinct IR absorption peaks.

FTIR is a common technique used to follow the radiolysis of IR absorbing molecules once it is sensitive to the number of precursor and product molecules in the sample. Since FTIR yields the column density of molecules that remain in the sample after irradiation, it is not possible to distinguish loss (disappearance) of molecules due to radiolysis from that due to sputtering. For molecular ices, because of radiolysis effect on the sample surface, it turns out that the sputtering yield also

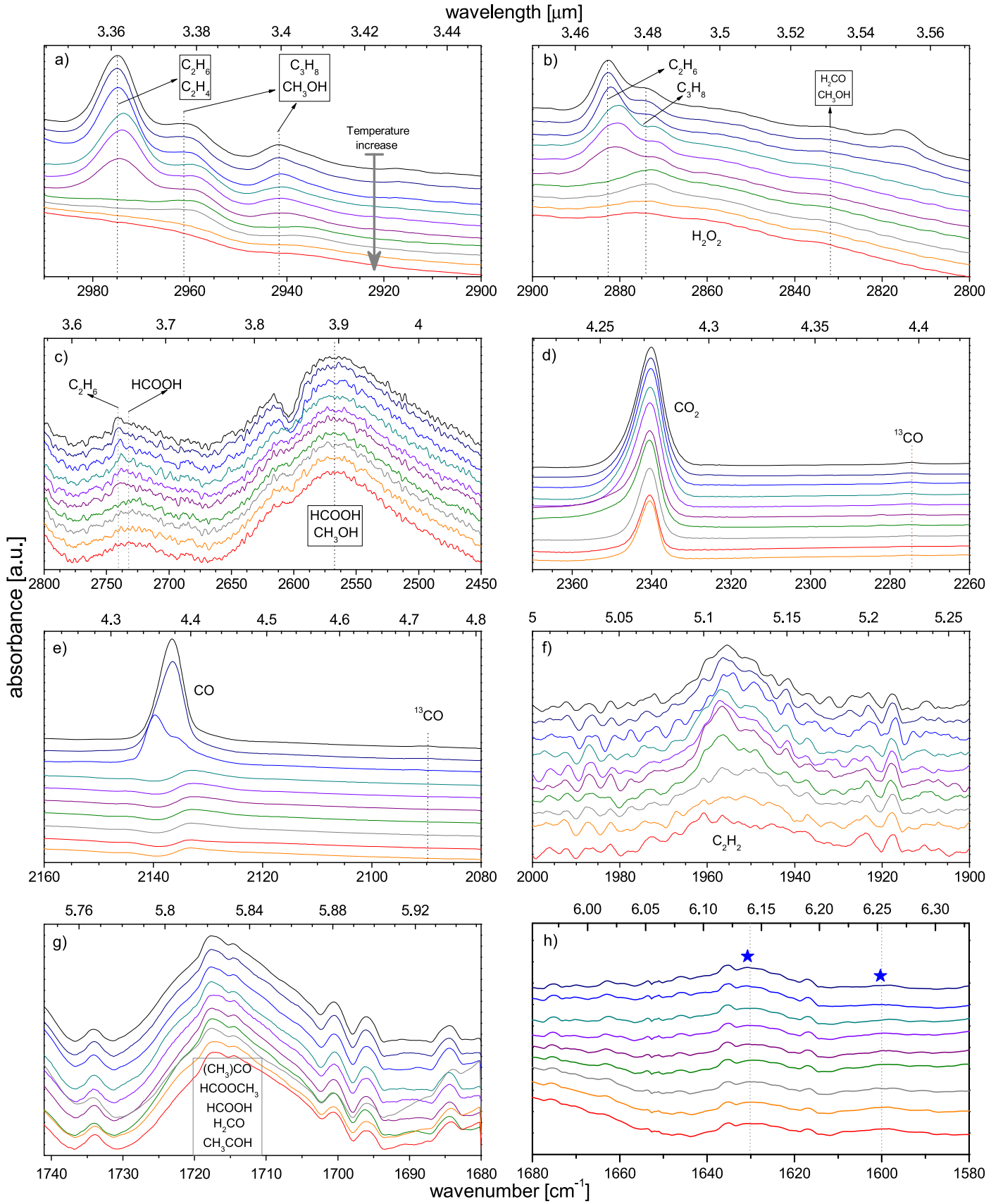

Figure 11. Dependence of the absorbance of irradiated CH_4:H_2O (1:3) ice on temperature. The upper lines correspond to colder ices; temperatures are the same as those shown in Figure 10. The vertical lines indicate the IR bands of synthesized molecules or groups of candidates with nearly the same band position. The IR sections correspond to different ranges as follows: panel (a): 2990–2900 cm^{-1}; panel (b): 2900–2800 cm^{-1}; panel (c): 2800–2480 cm^{-1}; panel (d): 2370–2260 cm^{-1}; panel (e): 2160–2080 cm^{-1}; panel (f): 2000–1900 cm^{-1}; panel (g): 1740–1680 cm^{-1}; and panel (h): 1680–1580 cm^{-1}. The blue stars indicate unidentified IR features.

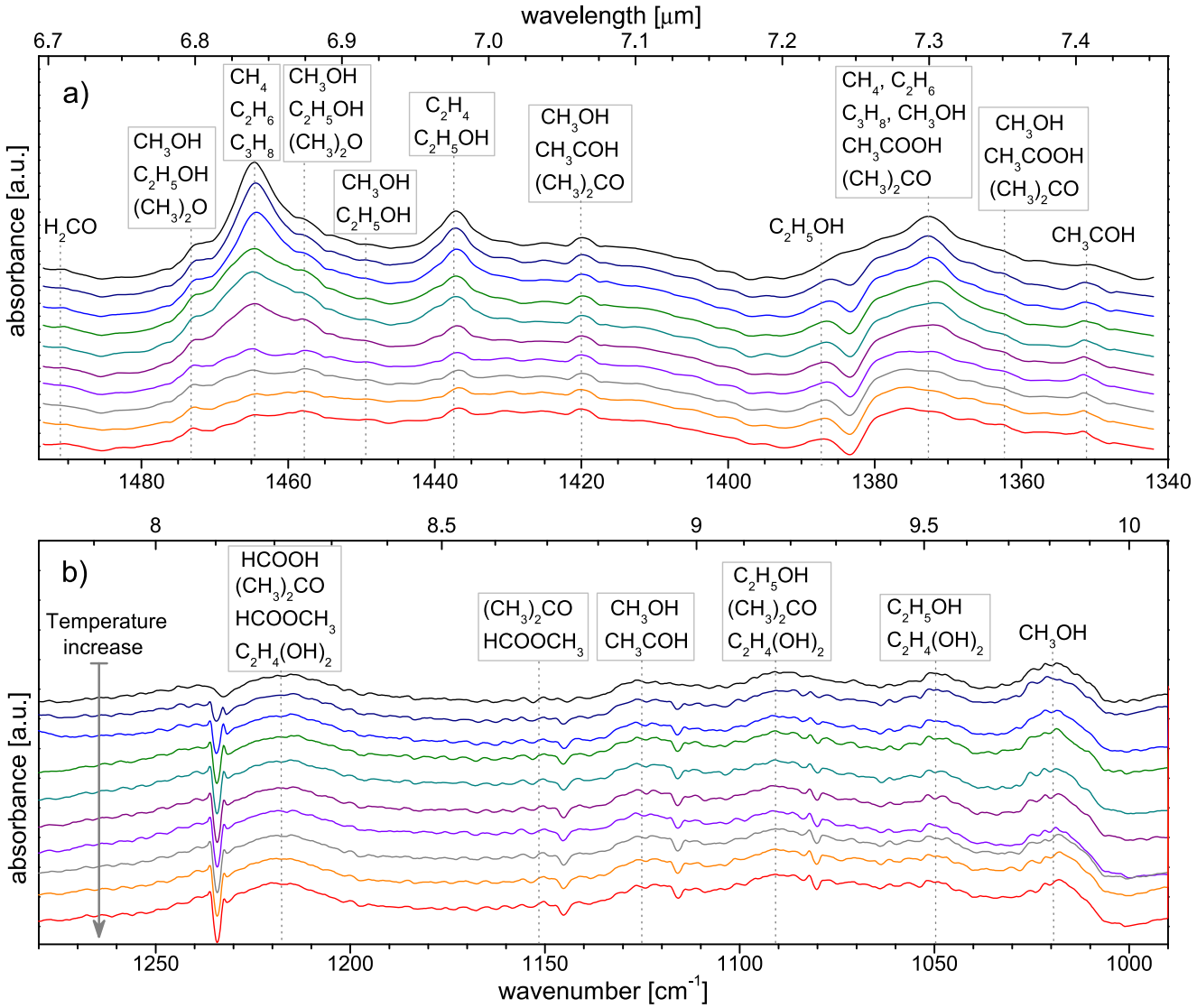

Figure 12. Evolution of IR absorption spectra of CH_4:H_2O (1:3) ice as temperature increases after irradiation. Panel (a) shows from 1495 to 1340 cm^{-1}, and panel (b) shows from 1280 to 990 cm^{-1}. Temperatures are the same as those in Figure 10, and the upper lines correspond to colder samples.

decreases exponentially with fluence, as column density usually does. If sputtering is not explicitly treated in the data analysis, the deduced destruction cross sections are overestimated. To account for this issue, a so-called "apparent" destruction cross section was introduced as a parameter corresponding to the sum of the two effects (Mejía et al. 2013). The results presented in Table 3 stem from such an analysis.

After the analysis of precursors, the column density evolutions of the radiolysis products are determined; using stoichiometry, the corresponding atomic column densities are calculated and summed up separately. With this procedure, FTIR informs how the number of atoms (per area unit) of each chemical element evolves as the precursor dissociation proceeds. Adding the obtained values to those of the remaining precursors, the number of atoms in the target for each atomic species is determined as a function of fluence. This number decreases linearly and its slope is the total (atomic) sputtering yield. The next step of data analysis is to estimate the molecular sputtering yield. This assessment is very rough since there is no information on the ejection of atoms or on the molecular structure of the sputtered species; assumptions need to be made. For instance, we may assume that most of the emitted molecules are intact precursors. Starting from total atomic sputtering yield for each element and, again, taking stoichiometry into account, the molecular sputtering yields are evaluated. This information, combined with the apparent cross-section value, gives the actual cross sections. A phenomenological model to compute these parameters is described in the following sections.

3.5.1. Cross Sections

During an arbitrary small irradiation time interval, dF projectiles impinge on a unit area of the sample surface. The number of target molecules of species i, by unit area and after the fluence F is, by definition, the molecular column density $N_i(F)$. If sputtering is negligible, the column density decrease dN_i of target molecules must be due to their destruction, i.e., fragmentation or chemical reactions; the destruction cross

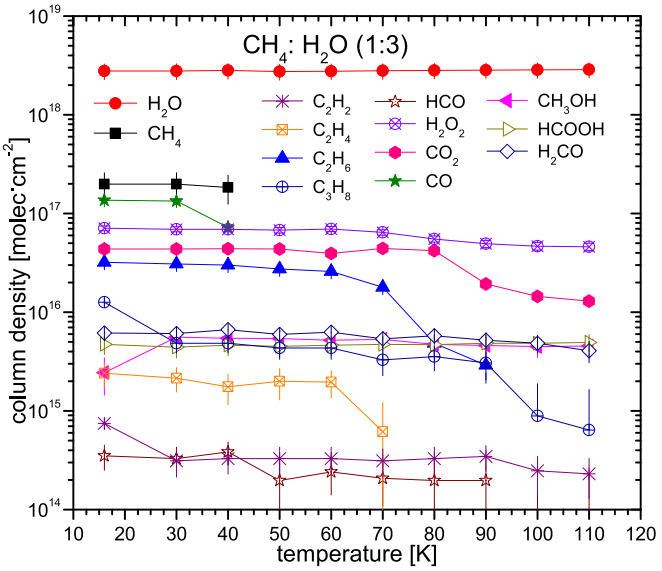

Figure 13. Evolution of column densities of precursors and products as the temperature of the irradiated (1:3) ice increases. The $^{58}Ni^{11+}$ beam fluence was 10^{13} ions cm^{-2}.

Table 3
Apparent Destruction and Formation Cross Sections (in 10^{-15} cm^2), Obtained by Fitting Low Fluence Data of Figures 1 and 3, for the (1:3) and (1:15) Ice Mixtures

Precursors	σ_d^{ap}(1:3)	σ_d^{ap}(1:15)	σ_d^{ap}(1:3)/σ_d^{ap}(1:15)
CH_4	120 ± 20	190 ± 30	0.63
H_2O	>20 ± 10	>17 ± 10	1.2
Products	σ_f(1:3)	σ_f(1:15)	σ_f(1:3)/σ_f(1:15)
C_2H_6	33 ± 7	2.8 ± 0.6	12
C_2H_4	1.1 ± 0.2	···	···
C_2H_2	0.04 ± 0.01	···	···
C_3H_8	1.5 ± 0.3	···	···
HCO	4.65 ± 0.9	···	···
H_2O_2	7.5 ± 4	17 ± 8	0.4
CO_2	1.1 ± 0.2	2.6 ± 0.5	0.4
CO	1.5 ± 0.3	1.3 ± 0.3	1.1
H_2CO	0.88 ± 0.2	0.75 ± 0.2	1.2
CH_3OH	7.8 ± 1.6	2.8 ± 1	2.8
HCOOH	1.7 ± 0.35	1 ± 0.4	1.7
CH_3CHO	20 ± 5	12 ± 4	1.7

Note. Since no sputtering correction has been considered, the precursor σ_d values are apparent for cross sections: $\sigma_d^{ap} = \sigma_d + Y_0/N_0$, for low fluences) (see the text); σ_d^{ap} errors are mainly due to fluence measurement. For the hydrocarbons formed in the (1:15) ice mixture, the cross-section determination was not possible. σ_d^{ap} for H_2O may be higher due to possible air leaking.

section of precursor molecules is, at that time, $\sigma_{d,i} = [dN_i(F)/dF]/N_i$. If no formation of this species occurs, one then has

$$N_i(F) = N_{0,i}e^{-\sigma_{d,i}F} \quad (1)$$

where $N_{0,i}$ is the initial column density of species i (i.e., N_{CH_4} or N_{H_2O} in the current work). If sputtering is nonnegligible and if experimental data do not allow for its distinction with radiolysis, the parameter $\sigma_{d,i}$ is called the apparent destruction cross section (see Section 3.5.2). For a given produced molecular species j, its formation cross section $\sigma_{f,j}$ and its destruction cross section $\sigma_{d,j}$ are connected by the relationship

$$\frac{dN_j(F)}{dF} = \sigma_{f,j}N_{k,j} - \sigma_{d,j}N_j \quad (2)$$

where $N_{k,j}$ is the column density of the N_j precursor. If there is just one precursor molecular species in the ice target, then $N_{kj} = N_i$. If there is a mixture of precursors, assumptions need to be made, taking into account the stoichiometry of each precursor and its relative abundances. Considering the data acquired at the beginning of irradiation, N_j is negligible, and $N_{k,j}$ is approximately constant and equal to the initial value $N_{0,kj}$. Equation (2) is then solved such that

$$N_j(F) \approx \sigma_{f,j}N_{0,kj}F. \quad (3)$$

Another approximation is to consider that $N_{k,j}$ is the same for all daughter molecules, N_k. In particular, this quantity may be the atomic column density $N_k^a = \Sigma_i n_i N_i$, where the molecular column densities N_i are weighted by the number of atoms n_i in each molecular species. For the studied system, $N_{0,k}^a = 5N_{0,CH_4} + 3N_{0,H_2O}$. This approximative solution was used to determine the $\sigma_{f,j}$ values presented in Table 3, using the daughter column densities at low fluences ($F < 10^{11}$ ions cm^{-2}).

We remind the reader that the existence of sputtering implies that precursor column densities decrease faster than predicted by Equation (1) (Seperuelo Duarte et al. 2009), giving the incorrect result that the destruction cross section is larger (Mejía 2013). For daughter species, the sputtering should reduce their formation cross sections; however, the approximations $N_j \approx 0$ and $N_{k,j} \approx N_{0,kj}$ eliminate the sputtering dependence terms in Equation (3).

3.5.2. Sputtering Yield

A new procedure for determining the atomic sputtering yield is proposed here, based on the column density evolution with beam fluence. The following conditions need to be taken into account:

(i) Since sputtering is a surface process, the sputtering yield should be constant provided that the sample composition stays constant during the irradiation. Very thin samples (thickness shorter than the sputtering depth) are excluded.
(ii) If chemical reactions occurs, molecular concentrations change, but—obviously—atomic concentrations do not.
(iii) In a first approximation, atomic sputtering yields are proportional to atomic concentrations. This should occur if the impact results in a high degree of atomization (near the projectile track) or on emission of intact precursors (far from the projectile track).
(iv) As a second approximation, atomic sputtering yields may depend on properties of the atomic and molecular species. For instance, light species such as hydrogen have a higher probability of escaping from the target than do heavy species.
(v) FTIR spectroscopy provides a determination of the sample molecular composition. Repeating this measurement for different fluences, the variation in the number of each molecular species is determined. Considering stoichiometry, this technique allows for the measurement of atomic sputtering yields. The fact that some products in the sample may be invisible to FTIR (e.g., free atoms

and homonuclear diatomic molecules) implies that this measurement is an upper limit. New experimental techniques are necessary to figure out the chemical and physical effects of heavy ion bombardment on ices, as has been mentioned by Rothard et al. (2017).

A formal treatment of this procedure for the case of J precursors, M_j, with $j = 1, J$, is presented. The atomic sputtering yield is determined by detecting the atoms ejected by impacts or by counting the decreasing number of atoms in the sample as the fluence evolves. The number of target atoms of the atomic species k per surface area at fluence F is, by definition, the atomic column density $N_k^a(F)$. The number of sputtered atoms of species k per surface area and during the fluence dF irradiation is $Y_k(F)\ dF$, where Y_0^a is the corresponding atomic sputtering yield. The conservation law for the number of atoms of any chemical element k can be written as

$$dN_k^a - Y_k^a dF = 0. \quad (4)$$

Assuming condition (iii), homogeneity is preserved, and Y_k^a does not depend of F. Solving Equation (4), we have

$$N_k^a(F) = N_{0,k}^a - Y_k^a F. \quad (5)$$

The total atomic column density, N^a(F), is obtained by summing Equation (5) for all atomic species: $N^a(\mathrm{F}) = \Sigma_k N_k^a(F)$. If $Y_0^a = \Sigma_k Y_{0,k}^a$ is the total atomic sputtering yield, then Equation (5) becomes

$$N^a(F) = N_0^a - Y_0^a F. \quad (6)$$

Alternatively, $N^a(F)$ can also be expressed in terms of M_j, the molecular column densities of N_j, the quantities measured by FTIR. It is necessary to have knowledge on the stoichiometry $n_{i,j}$, which represents the number of the element i in the precursor j: the atomic column density in the sample corresponding to the element i is $n_{i,j}\ N_j(F)$. Summing for all elements i and for all precursors j, Equation (6) becomes

$$N^a(F) = \sum_i \sum_j n_{i,j} N_j(F) = N_0^a - Y_0^a F. \quad (7)$$

Equation (7) shows explicitly that the angular coefficient of the function in $N^a(F)$ versus F plot gives the total atomic sputtering yield, as displayed in Figure 14.

Another approach consists of modeling the sputtering yield function $Y(F)$. Four typical situations may occur: (a) $Y(F) = Y_0$, a constant value; (b) $Y(F) = Y_0 \cdot \exp(-\sigma_d F)$; (c) $Y(F) = Y(F, \ell)$, where ℓ is the ice thickness; and (d) Y $(F) = Y\ (F, A)$, where A is the atomic number of target atoms. Situation (a) happens when the target surface composition does not change with fluence, e.g., samples are constituted by a single element, as silicon wafers or gold foils, or when all products sublimate, leaving the precursors without shielding at the surface. For single element targets, there is no radiolysis, and $N(F) = N_0 - Y_0 F$. Situation (b) corresponds to samples that are degraded by the ion beam and whose products stay in the surface, e.g., molecular ices as (C_2H_6:H_2O) (de Barros et al. 2016). In this case, precursor and daughter species concentrations at the sample surface decrease and increase exponentially, respectively. For low fluences, $N(F) = N_0 \cdot \exp(-\sigma_d^{\mathrm{ap}} F)$. For a large range of fluences,

$$N(F) = (N_0 - Y_0 F) e^{-\sigma_d F}. \quad (8)$$

Situation (c) is expected to occur for thin films having thicknesses smaller than the sputtering depth; Dartois et al. (2018) estimated that the sputtering yield depends exponentially on the ice thickness for values $<0.05\ \mu$m ($<1.2 \times 10^{17}$ molec cm^{-2}: this column density is much lower than those at the end of our experiment (around 2×10^{18} molec cm^{-2}). Situation (d) corresponds to materials with selective sputtering. For instance, light elements are more likely to be ejected by projectile impact, which causes intense hydrogen emission and surface enrichment of heavy elements; for alkali halide samples, the halide emission follows the electronic stopping while the alkali emission follows the electronic stopping power (Pereira et al. 1998).

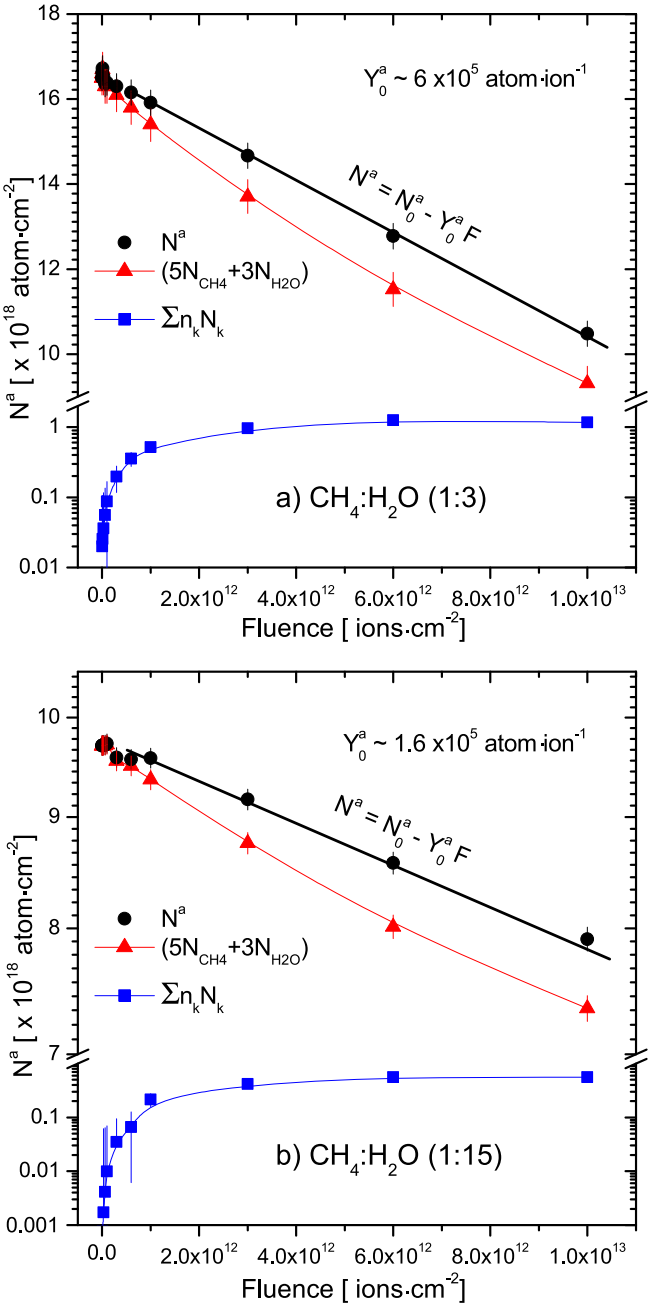

Figure 14. Total atomic column density evolution as a function of fluence. Triangles represent precursors, squares represent the most abundant products, and circles represent the total (sum). Panel (a) shows the (CH_4:H_2O) (1:3) ice, and panel (b) shows the (CH_4:H_2O) (1:15) ice. The total atomic sputtering yield Y_0^a for each ice mixture is determined from the best fit via Equation (7).

4. Discussion

4.1. Evolution of Porous Amorphous Ices

Four observed bands support the assumption that CH_4:H_2O ice produced by deposition at 15 K is a porous amorphous ice (see Section 3.1): (i) two water dangling bonds observed at 3684 and 3670 cm^{-1} (Palumbo 2006), and (ii) two methane bands at 2904 and 1530 cm^{-1} (Gerakines & Hudson 2015; Hudson et al. 2015). Bossa et al. (2015) found that the porosity of CH_4:H_2O ices depends on the ratio of CH_4 and H_2O concentrations; this means that the (1:3) ice contains more pores than the (1:15) ice. Both ice films were deposited with the same deposition rate, around 10 nm s^{-1}, which is also equal to the rate used in the current experiment (see Section 2).

The dangling bond features usually decrease under irradiation as first described by Palumbo (2006), Raut et al. (2008), and Palumbo et al. (2010). Dartois et al. (2013) found that the relationship between the compaction cross section (σ_c) and the electronic stopping powers (S_e) is $\sigma_c = S_e/D_0$ (with $D_0 = 0.2$ eV $molec^{-1}$). Mejía et al. (2015a) demonstrated that this relation is also valid for composite ices such as (CH_4:H_2O). The energy of 0.2 eV $molec^{-1}$ is close to the binding energy of the water molecule (Brill & Tippe 1967; Isaacs et al. 1999). For the $^{58}Ni^{11+}$ ion bombardment of (CH_4:H_2O) ice, the σ_c values for the (1:3) and (1:15) ices are 7.9 and 7.4 ($\times 10^{-12}$ cm^2), respectively. In turn, they correspond to the radii of 15.9 and 15.3 nm around the ion track, which define the volumes where the compaction process occurs. The electronic stopping powers for (1:3) and (1:15) ices are 1553 and 1475 ($\times 10^{-15}$ eV cm^2 $molec^{-1}$), respectively. Some physical and chemical processes that contribute to the compaction process upon ion impact on the ice film are as follows:

(i) The breaking of bonds caused by ionizations may lead to material modifications including atom dislocations, chemical reactions, and lattice structure rearrangement (Palumbo et al. 2010). Furthermore, the decrease of dangling bond features is correlated to internal displacement, which fills the void (pores) with sputtered material from internal surfaces. As an example, Oba et al. (2009) obtained compact amorphous water ice by co-deposition of hydrogen and oxygen ion atoms over porous water ice. Parent et al. (2002) estimated that cylindric pores have a diameter of 2 nm, separated by 0.6 nm, which could be filled with 385 molecules of water. These pores may be efficiently filled with the sputtered molecules ((5–16) $\times$ 10^4 molec ion^{-1}) by the $^{58}Ni^{11+}$ projectiles.

(ii) The chemical bond rupture can release UV photons with energies between 7.4 and 10.3 eV with a maximum penetration depth (into pure water ice at 8 K) around 180 nm (Cruz-Diaz et al. 2014). These UV photons generate secondary electrons that trigger chemical reactions, which induce ice compaction.

(iii) The molecular ionization triggers secondary electron (δ-electron) emission, provoking molecular ionization and/or excitations around the main ion track, which, in turn, would induce ice compaction. The δ-electrons, generated in liquid water by 1 MeV/nucleon ions, follow a distribution where the ratio between δ-electrons with energies of 10 eV and 1 keV is approximately 10^4 (for details see Rothard et al. 1996). The penetration depth of 10 keV δ-electron is about 100 nm (Nikjoo & Lindborg 2010).

Table 4
Precursor's Destruction Cross Sections and Initial Sputtering Yields

Ice Mixture	(1:3) Ice		(1:15) Ice	
Precursor	CH_4	H_2O	CH_4	H_2O
σ_d (10^{-15} cm^2)[a]	56 ± 12	···	170 ± 35	···
Y_0 (10^4 molec ion^{-1})[a]	8.5 ± 1.3	···	1.3 ± 0.2	···
σ_d^{ap} (10^{-15} cm^2)**	120 ± 20	18 ± 10	190 ± 30	17 ± 10
Y_0^a (10^4 atom ion^{-1}) ***	60 ± 10		16 ± 3	
Y_{total} (10^4 molec ion^{-1})[b]	17 ± 3		5 ± 1	
Y_0 (10^4 molec ion^{-1})[c]	4.3 ± 0.6	13 ± 2	0.32 ± 0.08	4.8 ± 0.7
N_0 (10^{18} molec cm^{-2})	1.2 ± 0.4	3.6 ± 0.5	0.20 ± 0.06	3.0 ± 0.4
Y_0/N_0 (10^{-15} cm^2)[d]	36 ± 6	36 ± 9	16 ± 5	16 ± 2
σ_d (10^{-15} cm^2)[e]	84 ± 35	(<0)	170 ± 55	(<1)

Notes.
[a] Values obtained with: *Equation (8), **Equation (1), ***Equation (6).
[b] $Y_{total} = [(a+b)/(aA+bB)]\,Y_0^a$;.
[c] $Y_0(A) = [a/(aA+bB)]\,Y_0^a$;.
[d] $Y_{total}/N_{0,total}(A) = Y_{total}/N_{0,total}(B) = Y_{total}/N_{0,total}$;.
[e] $\sigma_d = \sigma_d^{ap} - Y_0/N_0$: calculation using data of products and a sputtering model.

(iv) The passage of a projectile along the ice film increases the local temperature for a brief time. Such a temperature increase could explain the compaction process by inelastic thermal effects, as studied by Matsuzaki et al. (2017).

(v) The material ejected upon the impact of $^{58}Ni^{11+}$ ions on ice film produces craters, and dangling bonds could remain, as was suggested by de Barros et al. (2015).

(vi) The hydrogen produced may easily degas from the ice surface by leaving voids around the craters, as shown by Loeffler & Baragiola (2011). Besides that, the continuous hydrogen degassing (He et al. 2010) might create micropores near the ion track.

Other physical processes may contribute to the elimination of porosity, e.g., X-ray emission, Bremsstrahlung, and Compton scattering (Adlien & Adlyt 2017). Some exothermic chemical reactions between atoms or radicals could release thermal energy, e.g., the formation of methanol through the reaction $CH_3 + OH \rightarrow CH_3OH$ delivers 3.88 eV $molec^{-1}$ to the surroundings.

4.2. Radiolysis and Sputtering of the CH_4:H_2O Ice Film

The objective of this section is the determination of the CH_4 and H_2O destruction cross sections and sputtering yields for both ice mixtures. If the precursor's column densities are measured over a large fluence range, a direct procedure to extract σ_d and Y_0 consists of fitting their evolutions (displayed in Figures 8 and 9) with Equation (8) instead of Equation (1). The results are presented in Table 4. For CH_4, the fitting is straightforward and satisfactory. For H_2O, this method is not accurate: the decrease of H_2O column density for both ices is relatively low (~8%, up to $F = 10^{13}$ ion cm^{-2}), and only σ_d^{ap} could be extracted. Additional information on the column density of products is then necessary to proceed the analysis, which is done via the experimental data displayed in Figure 14.

Adding the column densities of precursors and identified products, an approximate linear decrease of the total atomic

column density is observed (Figures 14(a) and (b) for the 1:3 and 1:15 ice mixtures, respectively). The next step is to recognize that the constant Y_0^a, determined by fitting this linear decrease with Equation (6), is the maximum value of the total atomic sputtering yield. It is a maximum value because some partial column densities are missing in the sum $\sum n_k N_k$ (due to products not detectable by FTIR). The determined quantities Y_0^a are presented in the fourth line of Table 4.

In order to calculate the molecular sputtering yields, a model is needed. As discussed in Section 3.5.2, condition (iii), it is reasonable to assume that atomic sputtering yields are proportional to atomic concentrations. Considering that molecular species A (with A atoms) and B (with B atoms) form the A:B ice mixture with relative concentration a: b, inside a cell containing $(a + b)$ molecules, there are $(aA + bB)$ atoms. The molecular sputtering yield of species A (at least at the beginning of irradiation) is the fraction $a/(aA + bB)$ of Y_0^a. The total molecular sputtering yield is $Y_{\rm total} = [(a + b)/(aA + bB)]\,Y_0^a$. The results for the current ice mixtures are shown in Table 4.

Inspection of Table 4 shows the following:

1. Comparing CH_4 cross sections obtained directly from precursor's disappearance (first line) with those calculated from product's data treated by a model using condition (iii) (last line), a perfect agreement is found for the 1:15 ice mixture and a fair agreement (40%) for the 1:3 ice mixture.
2. The obtained H_2O cross sections are unsatisfactory for both mixtures. Even the apparent cross sections and the total atomic sputtering yields are too low for an ice mostly constituted by water. Atmospheric leaking is a possible explanation, but water condensation (from adsorbed molecules on the chamber walls) onto sample during the irradiation is more likely.
3. Comparing $\sigma_d^{\rm ap}$ with Y_0/N_0, one sees that CH_4 sputtering is responsible for 30% and 8.4% of the CH_4 removal from the 1:3 and 1:15 ice mixtures, respectively.
4. The fact the CH_4 was sputtered up to the end of the run excludes the possibility that a thick H_2O layer had condensed on the sample surface.

4.3. Dependence of Cross Sections on Stopping Power and Sputtering Yield on Stopping Power

Previous studies have reported how destruction cross sections evolve as a function of the electronic stopping power. For relatively low S_e values, measurements carried out by Moore & Hudson (1998) and Garozzo et al. (2011) indicate cross sections approximately constant over an S_e variation by a factor of 10. For high S_e values, results show a power dependence: $\sigma_d \approx aS_e^n$. The value of n differs according to the type of irradiated material, in particular, for carbonaceous material $0.9 < n < 1.7$ (Godard et al. 2011), in CH_3OH ice $n \approx 1.5$ (de Barros et al. 2011a), in CO_2 ice $n \sim 1$ (Mejía et al. 2015a), and for valine $n \sim 1$ (da Costa et al. 2020). Figure 15 presents the obtained CH_4 apparent destruction cross sections together with those from the literature: for CH_4:H_2O (1:x; with $x = 2,\ 7,\ 15$) irradiated by 0.8 MeV H^+ (Moore & Hudson 1998), and for CH_4:H_2O (1:4) irradiated by 30 keV He^+ (Garozzo et al. 2011). Figure 15 also shows that, for CH_4 molecules in the CH_4:H_2O ices, $\sigma_d^{\rm ap}$ is a function of S_e.

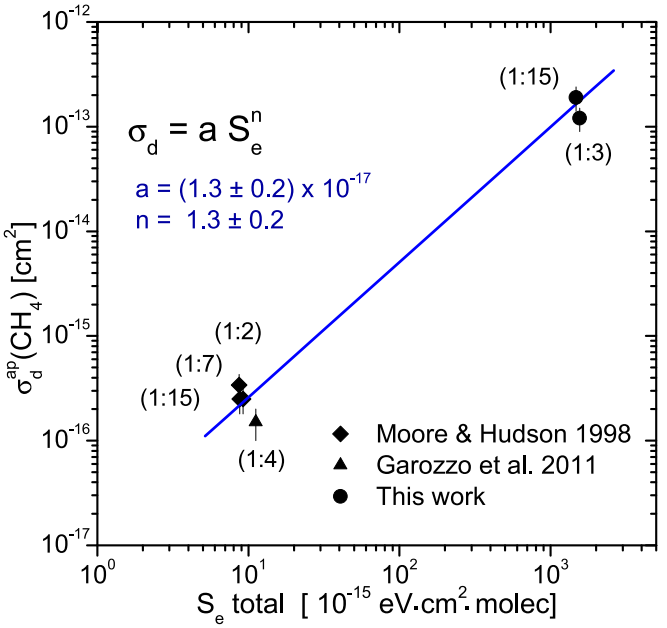

Figure 15. Apparent destruction cross sections of CH_4 molecules in the CH_4:H_2O ices as a function of the electronic stopping power. Results were reported by Moore & Hudson (1998), Garozzo et al. (2011), and obtained in this work (Table 3).

$$\sigma_d^{\rm ap} = aS_e^n \tag{9}$$

with the obtained fitting parameters $n = 1.3 \pm 0.2$ and $a = (1.3 \pm 0.2) \times 10^{-17}$ $[(10^{15}\,{\rm eV\,cm^2\,molec^{-1}})^{-1.3}\,{\rm cm^2}]$. One of the issues that emerges from the relation $\sigma_d^{\rm ap} \propto S_e^{1.3}$ is that for given projectile (40 MeV $^{58}Ni^{11+}$), $\sigma_d^{\rm ap}$ depends on the concentration of CH_4 molecules in the CH_4:H_2O ice.

The general conclusion to be drawn from Figure 15 is that distinct projectile-ice systems correspond to different cross sections. To measure the effect of all possible cosmic-ray ionic constituents at all energies is a huge task. However, it is possible to obtain scaling laws in S_e for a given ice (e.g., H_2CO, Figure 6 of de Barros et al. 2014b, and CH_3OH, Figure 8 of de Barros et al. 2012).

The use of such laws reduces enormously the mentioned task. For the case of ice mixtures (as for data displayed in Figure 15), stoichiometry is naturally taken into account in the stopping power calculations. However, cross sections are also sensitive to the variation of the chemical environment and, then, deviations of the power law may occur.

This explains why, as shown in Table 3, the ratio between the destruction cross sections for CH_4 increases by a factor ~2, while the ratio between both concentrations (1:3) and (1:15) decreases by a factor of four. The same argument may justify the dispersed cross sections values of CH_4 for different concentrations of CH_4:H_2O reported by Moore & Hudson (1998; Figure 15).

The sputtering yield, studied by Seperuelo Duarte et al. (2010) for pure CO ice, shows a quadratic dependence on the electronic stopping power: $Y_0 = \xi S_e^2$. Two other studies have confirmed this relation: crystalline water (Dartois et al. 2015)

Table 5
Carbon and Oxygen Budget for the (1:3) and (1:15) Ices after the Final Fluence (ff) of 10^{13} ion cm^{-2}

Ice Mixture	1:3 (Figure 8)		1:15 (Figure 9)	
Precursor	CH_4	H_2O	CH_4	H_2O
Atoms	C	O	C	O
a. N_0/N_{H_2O}	33	100	6.7	100
b. N_{ff}/N_{H_2O}	5.8	80	0.5	84.5
c. $\Delta N/N_{H_2O}$	−27	−20	−6.2	−15.5
d. $\sum N_k/N_{H_2O}$	8.8	11	5.7	14.5
e. $\Delta N/N_{H_2O}$	−18	−9	−0.5	−1.0

Note. Relative column densities (in %) are normalized to initial H_2O column density. Since there is a single carbon atom in CH_4 and a single oxygen atom in H_2O, the atomic and molecular column densities have the same value. Since the figures are relative column densities, errors are estimated to be ∼20%. Column density percentages: a. initial, b. final fluence, c. precursors, d. products, and e. missings.

and CO_2 (Mejía et al. 2015b), provided that ice thickness is >0.05 μm (Dartois et al. 2018).

4.4. Carbon and Oxygen Budget

The evolutions of column densities of molecules measured for the (1:3) and (1:15) ice mixtures are presented in Figures 8 and 9, respectively. Considering the stoichiometry of each molecular species, the evolutions of the column densities of H, C, and O atoms are determined and compared with initial quantities. H atoms, delivered in the bulk by CH_4 and H_2O radiolysis, escape partially from the sample as H or H_2, and their budget is not considered. The budget of C and O atoms is presented in Table 5. Note that there are three reasons for the imbalance:

(i) irradiation induces sputtering,

(ii) some molecular species may not be observed by FTIR (e.g., O_2), and

(iii) condensed molecules over the rear side of the substrate are detected by FTIR but are not processed by the ion beam (e.g., H_2O).

The sputtering process is formally treated in Section 3.5.2; results for the (1:3) and (1:15) ices are presented in Figures 14(a) and (b), respectively. Inaccuracy or impossibility to determine by FTIR the column density of single atoms and homonuclear molecules results in overestimating the sputtering yield; however, their contribution is expected to be relatively small in most cases. Condensed residual gases do not exceed 3×10^{15} molec cm^{-2} during the time required for one experiment (see Section 2).

5. Astrochemistry Considerations

5.1. Observation of Molecular Regions Rich in C, H, and O

Due to the ion beam energy, the results of the current work concern mainly cosmic-rays in the ISM and circumstellar envelopes; nevertheless, some conclusions on methane and water ice chemistry in the solar system and planetoids may be drawn. Also, comets were studied with flyby missions; IR and radio observations are used to measure the chemical composition of the gas and dust from their comae. A list of CHO-bearing species is presented in Table 6 (Mumma & Charnley 2011). CH_4 abundances, of 11 comets, vary from 0.4% to 2% relative to H_2O (Gibb et al. 2003; Paganini et al. 2014; Cochran et al. 2015; Goesmann et al. 2015).

Table 6 contains a list of molecules undetected by the instruments of Rosetta: HCO, C_3H_8, H_2O_2, C_2H_5OH, CH_3OCOOH, $(CH_3)_2CO$, $(CH_3)_2O$, and $HOCH_2CHO$ (Cochran et al. 2015). However, HCO^+ was observed in comet C/2012 S1 (ISON) around the Oort cloud (Agúndez et al. 2014); and C_2H_5OH was discovered in comet C/2014 Q2 (Lovejoy) (Cochran et al. 2015).

Table 6
Molecules Synthesized by CH_4:H_2O Irradiation and Also Observed on Solar System Planets, Their Satellites, and Outer Solar System Bodies or Planetoids (SSB-P), Comets (C), and the Interstellar Medium (ISM)

Molecule	SSB-P[a]	C[b]	ISM[c,d]
CH_4	1, 2, 3, 4, 5, 6, 7, 8, 9, 10 11, 12,13[e], 15, 16[e], 17, 18, 19	20[e] , 21, 22[e], 25	26
H_2O	3, 9, 11, 13[e], 16[e], 17, 18, 19, 46, 47	20[e], 21, 22[e], 25, 23[e]	27
HCO	…	24	28
C_2H_6	2, 5, 6, 8, 9, 10, 11, 15, 16[e], 17, 19	20[e], 22[e],	…
C_2H_4	8, 17	…	29
C_2H_2	6, 10, 17	21, 22[e],	30
C_3H_8	8	…	…
H_2O_2	47	…	31
CO_2	9, 10, 11, 13[e], 19	22[e], 25	32[e]
CO	9, 11, 12, 13[e], 14, 15, 16[e], 17, 18, 19	20[e], 21, 22, 25	33
H_2CO	…	21, 22[e], 23[e]	34
CH_3CHO	…	22[e], 25	35
CH_3OH	19	21, 22[e], 23[e]	36
C_2H_5OH	…	23	37
$C_2H_4(OH)_2$	…	22[e], 23[e]	38
HCOOH	…	22[e], 23[e]	39
CH_3OCOOH	…	…	40
$(CH_3)_2CO$	…	…	41
$HCOOCH_3$	…	22[e], 23[e]	42
$(CH_3)_2O$	…	…	43
$HOCH_2CHO$	…	22[e], 23[e], 25	44

Notes. The complete list of molecules in the solar system, comets, planetoids, and outer bodies, in addition to interstellar and circumstellar molecules can be found in.

[a] Klinger et al. (1986) and Gudipati & Castillo-Rogez (2013).

[b] Mumma & Charnley (2011).

[c] https://cdms.astro.uni-koeln.de/classic/molecules.

[d] http://www.astrochymist.org/astrochymist_mole.html.

[e] Molecules observed in solid phase.

References. (1) Krasnopolsky et al. (2004), (2) Krasnopolsky (2012), (3) Webster et al. (2015), (4) Wong et al. (2004), (5) Nixon et al. (2007), (6) Livengood et al. (1993), (7) Fletcher et al. (2009), (8) Brown et al. (2009), (9) Waite et al. (2006), (10) Burgdorf et al. (2006), (11) Holler et al. (2016), (12) Lellouch et al. (2011), (13) Quirico et al. (1999), (14) Encrenaz et al. (2004), (15) Meadows et al. (2008), (16) Cruikshank et al. (2015), (17) Gladstone et al. (2016), (18) Rivkin et al. (2015), (19) de Bergh et al. (2013), (20) Gibb et al. (2003), (21) Paganini et al. (2014), (22) Cochran et al. (2015), (23) Biver et al. (2015), (24) Agúndez et al. (2014), (26) Lacy et al. (1991), (27) Cheung et al. (1969), (28) Snyder et al. (1976), (29) Betz (1981), (30) Ridgway et al. (1976), (31) Bergman et al. (2011), (32) d'Hendecourt et al. (1989), (33) Wilson et al. (1970), (34) Snyder et al. (1969), (35) Gottlieb (1973), (36) Ball et al. (1970), (37) Zuckerman et al. (1975), (38) Hollis et al. (2002), (39) Zuckerman et al. (1971), (40) Mehringer et al. (1997), (41) Combes et al. (1987), (42) Brown et al. (1975), (43) Snyder et al. (1974), (44) Hollis et al. (2000).

Table 7
Molecular Abundances in Astrophysical Ices: Comets, MYSO, LYSO, BG Stars and in the Two Experiments Analyzed in This Paper

Specie	Comets[a,b]	LYSO[b]	MYSO[b]	BG Stars[b,c]	(1:3)[d]	(1:15)[d]
H_2O	100	100	100	100	100	100
CO	0.4–30	21^{35}_{12}	7^{15}_{4}	25^{43}_{20}	4.9	4.2
CO_2	2.5–30	28^{37}_{23}	19^{25}_{12}	26^{39}_{18}	1.6	3.2
CH_4	0.4–1.6	4.5^{6}_{3}	1–3	<3	7.2	0.61
C_2H_2	0.1–0.5	…	…	…	0.04	…
C_2H_6	0.1–2	…	…	…	1.16	0.03–0.16
CH_3OH	0.2–7	6^{12}_{5}	9^{23}_{5}	8^{10}_{6}	0.09	0.01–0.11
H_2O_2	2–17	…	…	…	0.45	3.2
H_2CO	0.11–4	~6	…	0.1–1	0.22	0.26
HCOOH	0.06–0.14	(<0.5)−4	(<0.5)−6	<2	0.17	0.30
CH_3CHO	0.002	…	…	…	<0.11	<0.09

Notes. The molecular abundances relative to H_2O were taken from.
[a] Cometary abundances, Mumma & Charnley (2011).
[b] Adapted from Boogert et al. (2015).
[c] Observations of background stars Öberg et al. (2011).
[d] This work, see the last irradiations in Figures 8 and 9. Since the values are relative column densities, errors are estimated to be ~20%.

Because high CH_4 concentrations have been found in some cold comets (temperatures below 40 K), the CH_4:H_2O ice mixture seems to be a good source of CHO-bearing compounds. It should be mentioned that the CH_4 molecule can coexist in clathrate hydrates until temperatures of 77 K (Dartois et al. 2010). Table 7 presents the molecular concentrations (relative to N_{H_2O}) for the (1:3) and (1:15) ices after irradiation corresponding to 15 eV molec^{-1} of deposited dose. The molecular percentages found in the present work are quantitatively consistent with those of the cometary ices; only few similarities with others astrophysical ices are noted.

Based on Tables 2 and 6, one can conclude that—except for C_2H_6 and C_3H_8 molecules—all of the synthesized species from irradiated CH_4:H_2O ices have also been observed in the ISM and circumstellar regions. Some of them were detected in the gas phase, but their origin is attributed to induced desorption by radiation or by sublimation from warmed grains. Molecules observed in the solid phase with CHO-bearing species are H_2O, CH_4, CO, CO_2, CH_3OH, H_2CO, HCOOH, and C_2H_5OH (Boogert et al. 2015). Analysis of the complex organic molecules, COMs, which are synthesized by ice irradiation, helps to figure out the chemical composition of the grain mantles in the ISM.

In the present work, the synthesis of CO, CO_2, CH_3OH, C_2H_5OH, H_2CO, HCOOH, and the likely occurrence of species CH_3CHO and CH_3OCOOH are discussed. The hydrocarbon production (C_2H_2, C_2H_4, C_2H_6, and C_3H_8) depends on CH_4 concentration. In contrast, the CH_4 destruction is higher at low CH_4 concentrations relative to H_2O as it was previously reported by Moore & Hudson (1998). This would support the idea that CH_4 at higher concentrations is more resistant to cosmic radiation: Figure 15 indeed reveals that, at least for high stopping powers, there has been a small decline in the destruction cross section of CH_4 as its concentration decreases. This finding could explain the observed solid CH_4 throughout the evolution of ices in the ISM and circumstellar envelopes.

The column density evolution of the radiolysis products during warming up shows IR bands that might belong to COMs (see Figures 11–13). COMs are expected to be produced in the cold clouds of the protostar. For example, in the YSO spectra corresponding to W 33A, IC1396α and HH 46 IRS objects (see Boogert et al. 2015, Figure 6) show IR absorptions that are similar to those of the candidate molecules depicted in Figure 12(b): C_2H_5OH (6.85, 6.97, 7.23 and 7.48 μm), CH_3OCOOH (6.08, 7.03 and 7.31 μm), $(CH_3)_2O$ (6.77 and 6.87 μm), C_2H_6 (6.83 and 7.27 μm), C_3H_8 (6.83 μm), C_2H_4 (6.96 μm), CH_3CHO (5.83, 7.02 and 7.41 μm), and $(CH_3)_2CO$ (7.02, 7.29 and 7.35 μm).

As mentioned in the Section 1, observations of icy mantles on grain surfaces, of diverse environments, have identified small molecules such as H_2O, CH_4, CO, CO_2, CH_3OH, and NH_3. The fragmentation of these simple molecules under ionizing radiation may result in the synthesis of complex molecules, COMs, in ice mantles on interstellar grains (Herbst & van Dishoeck 2009). Table 7 presents molecular species that have been observed in comets, High and Low Massive Young Stellar Objects (MYSOs and LYSOs), and Quiescent dense clouds. Ice percentages relative to H_2O are tabulated in Table 7. Molecular abundances from comets, measured in the gas phase, were taken from Mumma & Charnley (2011). The abundances for MYSO, LYSO, and for background star sources were adapted from Öberg et al. (2011) and Boogert et al. (2015). As expected, the percentages of CO, CO_2, and CH_3OH measured in Galactic sources differ from those obtained in the current experiment because, in space, CH_4 molecules are not considered as being their precursor (Dartois 2005). The CH_4 abundances considered in the present case are typical for comets and for interstellar sources. The hydrocarbon C_2H_2, found in comets, is produced in the irradiated (1:3) CH_4:H_2O ice, whereas C_2H_6 is formed in both (1:3) and (1:15) ices. This suggests that a link may exist between the CH_4 concentration and the C_2H_2 and C_2H_6 abundances, i.e., the hydrocarbons in the solid phase have not been detected in interstellar and circumstellar environments as a result of the local low CH_4 concentration.

The astronomical observations of CHO-bearing molecules tabulated in Tables 6 and 7 can be summarized as follows:

(i) The HCO molecule is believed to be formed over grain surfaces by hydrogenation of CO and also by gas interaction in gas-phase formation routes. HCO is found in gas phase around comets in the Oort cloud (Agúndez et al. 2014), in the dense molecular cloud Gerin et al. (2009). Bacmann & Faure (2016) proposed that the HCO

molecule, detected in prestellar cores, is synthesized on the grain surfaces.

(ii) *Hydrocarbons*. C_2H_2, C_2H_4, and C_2H_6 molecules have been detected in comets. C_2H_2 (Ridgway et al. 1976) and C_2H_4 (Betz 1981) have been found in the surroundings of circumstellar gas regions. Neither C_2H_6 nor C_3H_8 has been seen in the ISM.

(iii) *Peroxide*. Smith et al. (2011) demonstrated the existence of H_2O_2 in the mantles grains of molecular clouds of protostar with 9% N_{H_2O}.

(iv) *Carbon oxides*. CO and CO_2 are the most abundant observed molecules in the ISM other than H_2O and H_2 (Boogert et al. 2015). For example, Öberg et al. (2011) showed that their percentages (relative to N_{H_2O}) are approximately the same, as they are 29% and 13% (relative to N_{H_2O}) in the LYSO and the MYSO, respectively.

(v) *Aldehydes*. Gibb et al. (2004) observed the H_2CO and CH_3CHO molecules in solid phase from several sources of LYSOs, MYSOs, quiescent clouds, and diffuse ISM. H_2CO molecules were found with a percentage lower than 6% N_{H_2O}; the CH_3CHO feature at 1350 cm^{-1} (7.4 μm) overlaps with $HCOO^-$ (Öberg et al. 2011), making impossible the measurement of its column density.

(vi) *Alcohols*. CH_3OH is observed in almost all interstellar ices with an abundance from 0.5% to 5% of N_{H_2O} (Gibb et al. 2004). Gas and solid phase C_2H_5OH has been detected in diverse environments (see Bergantini et al. 2017, and references therein). Öberg et al. (2011) identified C_2H_5OH in cloud cores and in HYSO, but its feature overlaps with the HCOOH feature at 1384 cm^{-1} (7.25 μm) making hard their quantification. In the gas phase, $C_2H_4(OH)_2$ has been detected in the Galactic center by Hollis et al. (2000) and Requena-Torres et al. (2008).

(vii) *Acids*. HCOOH molecules were first observed in the ISM by Zuckerman et al. (1971), and their detection has been confirmed in diverse astrophysical environments ranging from molecular clouds to hot cores (Gibb et al. 2004; Knez et al. 2005; Requena-Torres et al. 2008; Boogert et al. 2011; Öberg et al. 2011). The HCOOH concentrations are lower than 6% N_{H_2O}, as shown in Table 7. CH_3OCOOH was first found in the ISM by Mehringer et al. (1997). Recently, observations from the observatory ALMA identified CH_3OCOOH in the envelopes surrounding of LYSO and in the hot core region of MYSO (Jørgensen et al. 2016 and Favre et al. 2017, respectively).

(viii) *Others*. The complex organic species $(CH_3)_2CO$, $HCOOCH_3$, and $(CH_3)_2O$ are found in distinct astrophysical environments in the gas phase (see Herbst & van Dishoeck 2009, and references therein). Observations have confirmed the existence of $(CH_3)_2CO$ (Lykke et al. 2017), $HCOOCH_3$ (Jørgensen et al. 2016), and $(CH_3)_2O$ (Jaber et al. 2014) in the envelope surrounding young protostar IRAS16293-2422.

Some of these species were formed in the ice mantles of grains of the prestellar or protostellar stage (Öberg et al. 2011). The most volatile molecules may be desorbed from the ices by protostellar ice heating. In the absence of heating, the astrophysical ice evolution may depend mostly on the sputtering process. The final section of this paper addresses the role of cosmic-rays to induce molecular desorption.

5.2. Sputtering Rates Under GCR Irradiation

Ices on dust grains are exposed continuously to Galactic Cosmic-Ray (GCR) bombardment, so that the chemical and physical structures of the ices evolve in time. The sputtering rates of these ices may be estimated by a procedure proposed by de Barros et al. (2011b) for radiolysis and applied by Dartois et al. (2015) for sputtering. For this calculation, the sputtering yield of ice mixtures is assumed to follow the quadratic dependence $Y_0 = \xi S_e^2$ (Seperuelo Duarte et al. 2010). Then, the sputtering rate η_{GCR} under GCR impact is given by

$$\eta_{GCR} = \sum_z \int\int Y_z(E_z)\Phi(E_z, \Omega) d\Omega dE_z$$
$$= 4\pi\xi \sum_z \int S_{e,z}^2(E_z) \frac{C_z E_z^{0.3}}{(E_z - E_0)^3} dE_z \quad (10)$$

where $\Phi(E_z, \Omega)$ is the flux density of the z ion, with z = H, He, C, O, Ne, Mg, Si, S, Ar, Ca, Fe, and Ni. Assuming an isotropic distribution of cosmic-rays, C_z is a parameter determined by the GRC abundances, and $S_{e,z}$ is the electronic stopping power of the ion z in the ice mixture. E_z is the projectile energy per nucleon, and E_0 is a form parameter for cosmic-ray distributions. The C_z and E_0 constants were taken from Shen et al. (2004) and Maurin et al. (2014). The lower and upper integration limits are 10^{-5} MeV nucleon^{-1} until 10^3 MeV nucleon^{-1}, outside of this region the integrad is considered zero.

Table 8 shows the predicted value of η_{GCR} for H_2O ice (Dartois et al. 2015), for CH_4 ice Mejía (2013), and CH_4:H_2O ices (this work), calculated for four E_0 values. As expected, for a given E_0, the η_{GCR} values for CH_4:H_2O (1:15 and 1:3) lie in between those for pure H_2O and CH_4 values.

Although light ions (H and He) are nearly 10^3 times more abundant than $^{58}Ni^{11+}$ or any other heavy ions in the GCR, the $^{58}Ni^{11+}$ sputtering rate is found to be 10 times higher than of light ions: $\eta_{Ni} \approx 10 \times \eta_{light}$ (with $\eta_{light} = \eta_H + \eta_{He}$). Interestingly, heavy ions dominate over light ions in the sputtering process induced by GCR. With regard to photodesorption, the UV photon flux is FUV $\approx 10^4$ photon cm^{-2} s^{-1} (Shen et al. 2004), and the photodesorption yield is $\eta_{FUV} \approx 10^{-3}$ molec photon^{-1} (Öberg et al. 2009). For the case of the composite (1:15) ice, a value of $\eta_{GCR} \approx 10^2$ molec cm^{-2} s^{-1} is obtained. The comparison of sputtering yields triggered by GCR versus UV photodesorption yields is

$$\frac{\eta_{GCR}}{\text{FUV}\eta_{FUV}} \approx 10. \quad (11)$$

This result indicates that the sputtering rate due to by GCR is higher than that of UV photodesorption process in the ISM grains mantles. Caution should be taken, since just a single type of ice mixture (CH_4:H_2O) was analyzed so far: conclusions should not be generalized a priori to all observed ices in the ISM (Boogert et al. 2015). A further study could assess the X effects in X:H_2O ices (with X = CO, CO_2, NH_3, CH_3OH, and other molecules) on the chemical and physical processes induced by GCR impact.

Considering molecular desorption, Boogert et al. (2004a) measured the H_2O and CH_4 column densities in the the

Table 8
Sputtering Rates (η_{GCR}, in molec cm^{-2} s^{-1}) for H_2O, CH_4:H_2O (1:15 and 1:3), and CH_4 Ices Under GCR Irradiation

Ice/E_0	200[a]	400[a]	600[a]	2000[b]
H_2O[c]	28	4.1	1.3	0.05
(1:15)[d]	168	25	7.9	0.31
(1:3)[d]	537	79	25	1.08
CH_4[e]	804	117	37	1.45

Notes. η_{GCR} was calculated following Equation (10) and by summing the contribution due to H, He, C, O, Ne, Mg, Si, S, Ar, Ca, Fe, and Ni projectile ions. Our different values of form parameter of cosmic-ray distribution (E_0, in MeV nucleon^{-1}) have been used.
[a] Shen et al. (2004).
[b] Maurin et al. (2014) (http://lpsc.in2p3.fr/crdb/#).
[c] From Dartois et al. (2015) for pure crystalline water ice.
[d] This work.
[e] From Mejía (2013) for pure methane ice.

protostar NGC 7538 IRS9. They found $N_{s,H_2O} \approx 7 \times 10^{18}$ molec cm^{-2} (in solid phase), $N_{s,CH_4} \approx 10^{17}$ molec cm^{-2} (in solid phase), and $N_{s,CH_4} \approx 2.3 \times 10^{16}$ molec cm^{-2} (in gaseous phase). Assuming that CH_4 in gas phase is produced from the ice mantles by the cosmic-rays sputtering process, their equivalent timescale to obtain N_{s,CH_4} may be estimated by

$$\tau_{g/s} \approx \frac{N_{s,CH_4}}{\eta_{GCR}}. \quad (12)$$

η_{GCR} is in the range of 1–10^2 molec cm^2 s^{-1}. The values of $\tau_{g/s}$ vary from 7 to 700 Ma. This range of time suggests that astrophysical gaseous CH_4 may originate from ices containing solid CH_4 via sputtering induced by cosmic-rays in the dose range from 1 to 10^2 eV molec^{-1}. Finally, it should be noted that the values of $\tau_{g/s}$ are smaller than dust lifetime in the ISM, i.e., about 4 Ga (Liffman & Clayton 1989); as a reference, the age of molecular clouds ranges in the 1–10 Ma interval (Pagani et al. 2012).

Part of this work was supported by the Direccion de Investigacion de la Universidad de Cuenca, DIUC. This work was supported by the French-Brazilian exchange program CAPES-COFECUB. The Brazilian agencies CNPq (INEspaço), Bolsa de Produtividade—CNPq (301868/2017-4), Projeto universal—CNPq (407938/2018-4), CAPES (BEX 5383/15-3), FINEP (0647/18), Cientista do Nosso Estado—FAPERJ (E-26/202.843/2018 and E-245307/(19) and FAPERJ (E-241202/18 and E-26/203.204/2017) are acknowledged.

ORCID iDs

C. Mejía https://orcid.org/0000-0001-7283-3421
A. L. F. de Barros https://orcid.org/0000-0001-7023-8282

References

Abplanalp, M. J., & Kaiser, R. I. 2020, ApJ, 889, 3
Adlien, D., & Adlyt, R. 2017, in Applications of Ionizing Radiation in Materials Processing, ed. Y. Sun & A. G Chmielewski (Warszawa: Inst. of Nuclear Chemistry and Technology), 55, http://www.ichtj.waw.pl/ichtj/publ/monogr/sun2017/sun-chapter3.pdf
Agúndez, M., Biver, N., Santos-Sanz, P. A., Bockelée-Morvan, D., & Moreno, R. 2014, A&A, 564, L2
Alexander, R. D., Casali, M. M., André, P., Persi, P., & Eiroa, C. 2003, A&A, 401, 613
Allamandola, L. J., Sandford, S. A., & Valero, G. J. 1988, Icar, 76, 225
Andrade, D. P., de Barros, A. L., Ding, J., et al. 2014, MNRAS, 444, 3792
Andrade, D. P., de Barros, A. L., Pilling, S., et al. 2013, MNRAS, 430, 787
Bacmann, A., & Faure, A. 2016, A&A, 587, A130
Ball, J. A., Gottlieb, C. A., Lilley, A. E., & Radford, H. E. 1970, ApJL, 162, L203
Baratta, G. A., Castorina, A. C., & Leto, G. 1994, P&SS, 42, 759
Bennett, C. J., Chen, S. H., Sun, B. J., Chang, A. H., & Kaiser, R. I. 2007, ApJ, 660, 1588
Bennett, C. J., Hama, T., Kim, Y. S., Kawasaki, M., & Kaiser, R. I. 2010, ApJ, 727, 27
Bennett, C. J., Jamieson, C. S., & Kaiser, R. I. 2009, PCCP, 11, 4210
Bennett, C. J., Jamieson, C. S., Osamura, Y., & Kaiser, R. I. 2005, ApJ, 624, 1097
Bennett, C. J., Jamieson, C. S., Osamura, Y., & Kaiser, R. I. 2006, ApJ, 653, 792
Bennett, C. J., & Kaiser, R. I. 2007, ApJ, 661, 899
Bennett, C. J., Pirim, C., & Orlando, T. M. 2013, ChRv, 113, 9086
Bergantini, A., Góbi, S., Abplanalp, M. J., & Kaiser, R. I. 2018, ApJ, 852, 70
Bergantini, A., Maksyutenko, P., & Kaiser, R. I. 2017, ApJ, 841, 96
Bergman, P., Parise, B., Liseau, R., et al. 2011, A&A, 531, L8
Betz, A. L. 1981, ApJL, 244, L103
Biver, N., Bockelée-Morvan, D., Moreno, R., et al. 2015, SciA, 1, e1500863
Boogert, A. A., Gerakines, P. A., & Whittet, D. C. 2015, ARA&A, 53, 541
Boogert, A. A., Pontoppidan, K. M., Lahuis, F., et al. 2004a, ApJS, 154, 359
Boogert, A. C., Blake, G. A., & Öberg, K. 2004b, ApJ, 615, 344
Boogert, A. C. A., Helmich, F. P., van Dishoeck, E. F., et al. 1998, A&A, 336, 352
Boogert, A. C. A., Huard, T. L., Cook, A. M., et al. 2011, ApJ, 729, 92
Boogert, A. C. A., Schutte, W. A., Helmich, F. P., Tielens, A. G. G. M., & Wooden, D. H. 1997, A&A, 317, 929
Boogert, A. C. A., Schutte, W. A., Tielens, A. G. G. M., et al. 1996, A&A, 315, L377
Bossa, J. B., Maté, B., Fransen, C., et al. 2015, ApJ, 814, 47
Brill, V. R., & Tippe, A. 1967, Acta Crystallographica, 23, 343
Brown, R., Lebreton, J. P., & Waite, H. (ed.) 2009, Titan from Cassini-Huygens (Dordrecht: Springer)
Brown, R. D., Crofts, J. G., Gardner, F. F., et al. 1975, ApJL, 197, L29
Brunetto, R., Caniglia, G., Baratta, G. A., & Palumbo, M. E. 2008, ApJ, 686, 1480
Burgdorf, M., Orton, G., van Cleve, J., Meadows, V., & Houck, J. 2006, Icar, 184, 634
Cheung, A. C., Rank, D. M., Townes, C. H., Thornton, D. D., & Welch, W. 1969, Natur, 221, 626
Chiar, J. E., Adamson, A. J., Pendleton, Y. J., et al. 2002, ApJ, 570, 198
Chiar, J. E., Tielens, A. G. G. M., Whittet, D. C. B., et al. 2000, ApJ, 537, 749
Cochran, A. L., Levasseur-Regourd, A. C., Cordiner, M., et al. 2015, SSRv, 197, 9
Combes, F., Gerin, M., Wootten, A., et al. 1987, A&A, 180, L13
Comeford, J. J., & Gould, J. H. 1961, JMoSp, 5, 474
Cottin, H., Moore, M. H., & Bénilan, Y. 2003, ApJ, 590, 874
Cruikshank, D. P., Grundy, W. M., DeMeo, F. E., et al. 2015, Icar, 246, 82
Cruz-Diaz, G. A., Caro, G. M., Chen, Y. J., & Yih, T. S. 2014, A&A, 562, A119
da Costa, C. A., Muniz, G. S. V., Boduch, P., Rothard, H., & Silveira, E. F. D. 2020, Int. J. Mol. Sci., 21, 1893
d'Hendecourt, L., Jourdain de Muizon, M., Dartois, E., et al. 1996, A&A, 315, L365
d'Hendecourt, L. B., & Jourdain de Muizon, M. 1989, A&A, 223, L5
Dartois, E. 2005, ISO Science Legacy, The Ice Survey Opportunity of ISO (Dordrecht: Springer), 293
Dartois, E., Augé, B., Boduch, P., et al. 2015, A&A, 576, A125
Dartois, E., Chabot, M., Barkach, T. I., et al. 2018, A&A, 618, A173
Dartois, E., Deboffle, D., & Bouzit, M. 2010, A&A, 514, A49
Dartois, E., D'Hendecourt, L. B., Boulanger, F., et al. 1998, A&A, 331, 651
Dartois, E., Ding, J. J., de Barros, A. L. F., et al. 2013, A&A, 557, A97
de Barros, A. L. F., Boduch, P., Domaracka, A., Rothard, H., & da Silveira, E. F. 2012, LTP, 38, 759
de Barros, A. L. F., Bordalo, V. S. D. E., Duarte, E. S., et al. 2011a, A&A, 531, A160
de Barros, A. L. F., da Silveira, E. F., Fulvio, D., Rothard, H., & Boduch, P. 2016, ApJ, 824, 81
de Barros, A. L. F., da Silveira, E. F., Pilling, S., et al. 2014a, MNRAS, 438, 2026
de Barros, A. L. F., da Silveira, E. F., Rothard, H., Langlinay, T., & Boduch, P. 2014b, MNRAS, 443, 2733

de Barros, A. L. F., Domaracka, A., Andrade, D. P. P., et al. 2011b, MNRAS, 418, 1363
de Barros, A. L. F., Mejía, C., Morgado, W. A. M., Almeida, L. F., & da Silveira, E. F. 2015, BrJPh, 45, 195
de Bergh, C., Schaller, E. L., Brown, M. E., et al. 2013, The Science of Solar System Ices (New York: Springer), 107
Encrenaz, T., Lellouch, E., Drossart, P., et al. 2004, A&A, 413, L5
Favre, C., Pagani, L., Goldsmith, P. F., et al. 2017, A&A, 604, L2
Fletcher, L. N., Orton, G. S., Teanby, N. A., Irwin, P. G. J., & Bjoraker, G. L. 2009, Icar, 199, 351
Gálvez, Ó, Maté, B., Herrero, V. J., & Escribano, R. 2009, ApJ, 703, 2101
Garozzo, M., la Rosa, L., Kanuchova, Z., et al. 2011, A&A, 528, A118
Gerakines, P. A., & Hudson, R. L. 2015, ApJL, 805, L20
Gerin, M., Goicoechea, J. R., Pety, J., & Hily-Blant, P. 2009, A&A, 494, 977
Gibb, E. L., Mumma, M. J., Russo, N. D., DiSanti, M. A., & Magee-Sauer, K. 2003, Icar, 165, 391
Gibb, E. L., Whittet, D. C. B., Boogert, A. C. A., & Tielens, A. G. G. M. 2004, ApJS, 151, 35
Gibb, E. L., Whittet, D. C. B., Schutte, W., et al. 2000, ApJ, 536, 347
Gladstone, G. R., Stern, S. A., Ennico, K., et al. 2016, Sci, 351, aad8866
Godard, M., Féraud, G., Chabot, M., et al. 2011, A&A, 529, A146
Goesmann, F., Rosenbauer, H., Bredehöft, J. H., et al. 2015, Sci, 349, aab0689
Gottlieb, C. A. 1973, Molecules in the Galactic Environment (New York: Wiley), 181
Graninger, D. M., Wilkins, O. H., & Öberg, K. I. 2016, ApJ, 819, 140
Gudipati, M. S., & Castillo-Rogez, J. 2013, The Science of Solar System Ices, Astrophysics and Space Science Library, Vol. 356 (New York: Springer)
Gürtler, J., Klaas, U., Henning, T., et al. 2002, A&A, 390, 1075
Hagen, W., Tielens, A. G. G. M., & Greenberg, J. M. 1981, CP, 56, 367
He, J., Gao, K., Vidali, G., Bennett, C. J., & Kaiser, R. I. 2010, ApJ, 721, 1656
Herbst, E., & van Dishoeck, E. F. 2009, ARA&A, 47, 427
Hodyss, R., Johnson, P. V., Stern, J. V., Goguen, J. D., & Kanik, I. 2009, Icar, 200, 338
Holler, B. J., Young, L. A., Grundy, W. M., & Olkin, C. B. 2016, Icar, 267, 255
Hollis, J. M., Lovas, F. J., & Jewell, P. R. 2000, ApJL, 540, L107
Hollis, J. M., Lovas, F. J., Jewell, P. R., & Coudert, L. H. 2002, ApJL, 571, L59
Hudson, R., Moore, M., Gerakines, P., et al. 2019, in The Cosmic Ice Laboratory - IR Spectra (Greenbelt, MD: Goddard Space Flight Center), https://science.gsfc.nasa.gov/691/cosmicice/spectra.html
Hudson, R. L., Gerakines, P. A., & Loeffler, M. J. 2015, PCCP, 17, 12545
Hudson, R. L., & Moore, M. H. 1999, Icar, 140, 451
Isaacs, E. D., Shukla, A., Platzman, P. M., et al. 1999, PhRvL, 82, 600
Jaber, A. A., Ceccarelli, C., Kahane, C., & Caux, E. 2014, ApJ, 791, 29
Jamieson, C. S., Mebel, A. M., & Kaiser, R. I. 2006, ApJS, 163, 184
Jørgensen, J. K., van der Wiel, M. H. D., Coutens, A., et al. 2016, A&A, 595, A117
Klinger, J., Benest, D., Dollfus, A., & Smoluchowski, R. 1986, JBAA, 96, 358
Knez, C., Boogert, A. A., Pontoppidan, K. M., et al. 2005, ApJL, 635, L145
Knez, C., Moore, M. H., Ferrante, R. F., & Hudson, R. L. 2012, ApJ, 748, 95
Krasnopolsky, V. A. 2012, Icar, 217, 144
Krasnopolsky, V. A., Maillard, J. P., & Owen, T. C. 2004, Icar, 172, 537
Lacy, J. H., Carr, J. S., Evans, N. J., et al. 1991, ApJ, 376, 556
Lellouch, E., de Bergh, C., Sicardy, B., Käufl, H. U., & Smette, A. 2011, A&A, 530, L4
Liffman, K., & Clayton, D. D. 1989, ApJ, 340, 853
Livengood, T. A., Kostiuk, T., Espenak, F., & Goldstein, J. J. 1993, JGRE, 98, 18813
Loeffler, M. J., & Baragiola, R. A. 2011, ApJ, 744, 102
Loeffler, M. J., Raut, U., Vidal, R. A., Baragiola, R. A., & Carlson, R. W. 2006a, Icar, 180, 265
Loeffler, M. J., Teolis, B. D., & Baragiola, R. A. 2006b, JChPh, 124, 104702
Lykke, J. M., Coutens, A., Jørgensen, J. K., et al. 2017, A&A, 597, A53
Matsuzaki, S., Hayashi, H., Nakajima, K., et al. 2017, NIMPB, 406, 456
Maurin, D., Melot, F., & Taillet, R. 2014, A&A, 569, A32
Meadows, V. S., Orton, G., Line, M., et al. 2008, Icar, 197, 585
Mehringer, D. M., Snyder, L. E., Miao, Y., & Lovas, F. J. 1997, ApJL, 480, L71
Mejía, C., Bender, M., Severin, D., et al. 2015a, NIMPB, 365, 477
Mejía, C., de Barros, A. L. F., Duarte, E. S., et al. 2015b, Icar, 250, 222
Mejía, C. F., de Barros, A. L. F., Bordalo, V., et al. 2013, MNRAS, 433, 2368
Mejía, G. C. F. 2013, PhD thesis, Pontificia Universidade Catolica do Rio de Janeiro
Moore, M. H. 1981, PhD thesis, Univ. Maryland
Moore, M. H., & Hudson, R. L. 1998, Icar, 135, 518
Mumma, M. J., & Charnley, S. B. 2011, ARA&A, 49, 471
Nikjoo, H., & Lindborg, L. 2010, PMB, 55, R65
Nixon, C. A., Achterberg, R. K., Conrath, B. J., et al. 2007, Icar, 188, 47
Noriega-Crespo, A., Morris, P., Marleau, F. R., et al. 2004, ApJS, 154, 352
Oba, Y., Miyauchi, N., Hidaka, H., et al. 2009, ApJ, 701, 464
Öberg, K. I., Boogert, A. A., Pontoppidan, K. M., et al. 2008, ApJ, 678, 1032
Öberg, K. I., Boogert, A. A., Pontoppidan, K. M., et al. 2011, ApJ, 740, 109
Öberg, K. I., Garrod, R. T., van Dishoeck, E. F., & Linnartz, H. 2009, A&A, 504, 891
Öberg, K. I., van Dishoeck, E. F., Linnartz, H., & Andersson, S. 2010, ApJ, 718, 832
Pagani, L., Lesaffre, P., Roueff, E., et al. 2012, RSPTA, 370, 5200
Paganini, L., Mumma, M. J., Villanueva, G. L., et al. 2014, ApJ, 791, 122
Palumbo, M. E. 2006, A&A, 453, 903
Palumbo, M. E., Baratta, G. A., Brucato, J. R., et al. 1998, A&A, 334, 247
Palumbo, M. E., Baratta, G. A., Leto, G., & Strazzulla, G. 2010, JMoSt, 972, 64
Parent, P., Laffon, C., Mangeney, C., Bournel, F., & Tronc, M. 2002, JChPh, 117, 10842
Pereira, J. A. M., Bitensky, I. S., & da Silveira, E. F. 1998, IJMSI, 174, 179
Ponciano, C. R., Martinez, R., Farenzena, L. S., et al. 2006, JASMS, 17, 1120
Quirico, E., Douté, S., Schmitt, B., et al. 1999, Icar, 139, 159
Raut, U., Famá, M., Loeffler, M. J., & Baragiola, R. A. 2008, ApJ, 687, 1070
Requena-Torres, M. A., Martín-Pintado, J., Martín, S., & Morris, M. R. 2008, ApJ, 672, 352
Ridgway, S. T., Hall, D. N., Kleinmann, S. G., Weinberger, D. A., & Wojslaw, R. S. 1976, Natur, 264, 345
Rivkin, A. S., Campins, H., Emery, J. P., et al. 2015, Asteroids IV (Tucson, AZ: Univ. Arizona Press), 65
Rocha, W. R. M., & Pilling, S. 2014, Spectrochim. Acta A, 123, 436
Rothard, H., Domaracka, A., Boduch, P., et al. 2017, JPhB, 50, 062001
Rothard, H., Jung, M., Gervais, B., et al. 1996, NIMPB, 107, 108
Seperuelo Duarte, E., Boduch, P., Rothard, H., et al. 2009, A&A, 502, 599
Seperuelo Duarte, E., Domaracka, A., Boduch, P., et al. 2010, A&A, 512, A71
Shen, C. J., Greenberg, J. M., Schutte, W. A., & van Dishoeck, E. F. 2004, A&A, 415, 203
Smith, R. G., Charnley, S. B., Pendleton, Y. J., et al. 2011, ApJ, 743, 131
Snyder, L. E., Buhl, D., Schwartz, P. R., et al. 1974, ApJL, 191, L79
Snyder, L. E., Buhl, D., Zuckerman, B., & Palmer, P. 1969, PhRvL, 22, 679
Snyder, L. E., Hollis, J. M., & Ulich, B. L. 1976, ApJL, 208, L91
Spoon, H. W. W., Keane, J. V., Tielens, A. G. G. M., Lutz, D., & Moorwood, A. F. M. 2001, A&A, 365, L353
Stief, L. J., Decarlo, V. J., & Hillman, J. J. 1965, JChPh, 43, 2490
Suhasaria, T., Thrower, J. D., Frigge, R., et al. 2018, PCCP, 20, 7457
Tanabashi, M., Hagiwara, K., Hikasa, K., Nakamura, K., et al. 2018, PhRvD, 98, 030001
Thompson, W. R., Murray, B. G. J. P. T., Khare, B. N., & Sagan, C. 1987, JGRA, 92, 14933
van Dishoeck, E. F., Bergin, E. A., Lis, D. C., & Lunine, J. I. 2014, in Protostars and Planets VI, ed. H. Beuther et al. (Tucson, AZ: Univ. Arizona Press), 835
van Dishoeck, E. F., Herbst, E., & Neufeld, D. A. 2013, ChRv, 113, 9043
Wada, A., Mochizuki, N., & Hiraoka, K. 2006, ApJ, 644, 300
Waite, J. H., Combi, M. R., Ip, W. H., et al. 2006, Sci, 311, 1419
Webster, C. R., Mahaffy, P. R., Atreya, S. K., et al. 2015, Sci, 347, 415
White, G. J., Liseau, R., Men'schikov, A., et al. 2000, A&A, 364, 741
Wilson, R. W., Jefferts, K. B., & Penzias, A. A. 1970, ApJL, 161, L43
Wong, M. H., Mahaffy, P. R., Atreya, S. K., Niemann, H. B., & Owen, T. C. 2004, Icar, 171, 153
Zasowski, G., Kemper, F., Watson, D. M., et al. 2009, ApJ, 694, 459
Ziegler, J. F., Ziegler, M. D., & Biersack, J. P. 2010, NIMPB, 268, 1818
Zuckerman, B., Ball, J. A., & Gottlieb, C. A. 1971, ApJL, 163, L41
Zuckerman, B., Turner, B. E., Johnson, D. R., et al. 1975, ApJL, 196, L99